nature portfolio

https://doi.org/10.1038/s41586-024-07534-6

Supplementary information

Explainable El Niño predictability from climate mode interactions

In the format provided by the authors and unedited

Supplementary Information for "Explainable El Niño predictability from climate mode interactions"

Sen Zhao[1], Fei-Fei Jin[1,2], Malte F. Stuecker[2,3], Philip R. Thompson[3], Jong-Seong Kug[4], Michael J. McPhaden[5], Mark A. Cane[6], Andrew T. Wittenberg[7], Wenju Cai[8,9,10,11]

[1] *Department of Atmospheric Sciences, School of Ocean and Earth Science and Technology (SOEST), University of Hawai'i at Mānoa, HI, USA*
[2] *International Pacific Research Center, SOEST, University of Hawai'i at Mānoa, Honolulu, HI, USA*
[3] *Department of Oceanography, SOEST, University of Hawai'i at Mānoa, Honolulu, HI, USA*
[4] *School of Earth and Environmental Sciences, Seoul National University, Seoul, South Korea*
[5] *National Oceanic and Atmospheric Administration (NOAA)/Pacific Marine Environmental Laboratory, Seattle, WA, USA*
[6] *Lamont Doherty Earth Observatory of Columbia University, Palisades, NY, USA*
[7] *NOAA/OAR/Geophysical Fluid Dynamics Laboratory, Princeton, NJ, USA*
[8] *Frontiers Science Center for Deep Ocean Multispheres and Earth System, Physical Oceanography Laboratory, and Sanya Oceanographic Institution, Ocean University of China, Qingdao, China*
[9] *Laoshan Laboratory, Qingdao, China*
[10] *State Key Laboratory of Loess and Quaternary Geology, Institute of Earth Environment, Chinese Academy of Sciences, Xi'an, China*
[11] *State Key Laboratory of Marine Environmental Science & College of Ocean and Earth Sciences, Xiamen University, Xiamen, China*

Correspondence and requests for materials should be addressed to Fei-Fei Jin (jff@hawaii.edu)

Contents:

Supplementary Text

Supplementary Text 1. Efficacy of the XRO in simulating ENSO and other climate modes

First, the XRO captures the observed seasonal synchronization of ENSO, with the Niño3.4 SSTA standard deviation peaking in November-December-January (Fig. 2a). This seasonal synchronization is primarily governed by the seasonal modulation of the SSTA growth rate due to the tropical Pacific background seasonal cycle (*Stein et al. 2014*; *Chen and Jin 2021*; *Levine and McPhaden 2015*). Second, the XRO successfully replicates El Niño-La Niña asymmetry, manifesting as positively skewed Niño3.4 SSTAs (Fig. 2b). This asymmetry arises from multiple nonlinear physical processes, such as oceanic nonlinear dynamical heating (*An and Jin 2004*; *An et al. 2020*) and nonlinear SST-wind stress coupling due to the nonlinear dependence of deep convection on SST (*Kang and Kug 2002*; *Choi et al. 2013*; *Geng et al. 2020*). Third, the observed ENSO periodicity is reasonably captured, with a Niño3.4 spectral peak at periods of 2-6 years (Fig. 2c).The XRO also captures the lead-time of warm water volume (WWV) anomaly ahead of ENSO SSTA by approximately 6-9 months (Fig. 2d), which is largely controlled by ENSO periodicity (*Zhao et al. 2021*). Fourth, the XRO generates the observed irregular interannual oscillations between El Niño and La Niña, including occurrences of single- and multi-year ENSO events (Supplementary Fig. 3). Various mechanisms governing multi-year ENSO occurrences have been well-documented, including nonlinearity (*Okumura et al. 2011*; *DiNezio and Deser 2014*), ENSO-combination mode and anomalous Ekman transport (*Iwakiri and Watanabe 2021*, *2022*), the NPMM and North Pacific Oscillation (*Ding et al. 2022*; *Geng et al. 2023*; *Park et al. 2021*; *Kim et al. 2023*), as well as inter-basin interactions with tropical Indian and/or Atlantic Oceans (*Kim and Yu 2022*). Notably, the XRO model incorporates all these elements either explicitly or implicitly (See *"Extended Nonlinear Recharge-Oscillator model (XRO)" in Methods*). Fifth, the XRO accurately reproduces the rapid decline in ENSO SSTA autocorrelation across boreal spring, commonly referred to as the spring persistence barrier (Supplementary Fig. 4).

The XRO reproduces the seasonal synchronization of the other climate modes that is seen in observations (Supplementary Fig. 5a-h), which in this model is largely caused by the seasonally varying damping rates of the individual modes, together with their coupled interactions (see diagonal axis in Extended Data Fig. 1). Notably, ENSO-driven processes play a pronounced role in the seasonal synchronization of some of the modes. For instance, the IOB warming, forced by El Niño, reaches its mature phase during boreal spring and summer, following the mature phase of El Niño (Supplementary Fig. 5c). The variance of the TNA peaks in boreal spring, due to both the seasonal modulation of its damping rate and the remote forcing from ENSO (*Chen et al. 2021*; *Jiang et al. 2023*). Moreover, the XRO reasonably reproduces the observed asymmetries of both the IOB and IOD, manifesting as positively skewed SSTAs in the central and western tropical Indian Ocean, and negatively skewed SSTAs in the eastern Indian Ocean near Java and Sumatra (Supplementary Fig. 5k-l). The positive skewness of the IOB primarily arises as a response to the skewed remote forcing from ENSO, while the IOD asymmetry is dominated by local nonlinear processes (*An et al. 2023*). Furthermore, the XRO accurately reproduces the observed seasonal autocorrelation of the other modes (Supplementary Fig. 6).

Supplementary Tables

Supplementary Table 1. Definition of SST indices for climate modes used in the study.

Climate Mode	Acronym	Description	References
El Niño-Southern Oscillation	ENSO	SSTAs averaged over Niño3.4 region 170°–120°W, 5°S–5°N	(*Trenberth 1997*)
North Pacific Meridional Mode	NPMM	SSTAs averaged over 160°-120°W, 10°-25°N	(*Richter et al. 2022*)
South Pacific Meridional Mode	SPMM	SSTAs averaged over 110°-90°W, 25°-15°S	(*Zhang et al. 2014*)
Indian Ocean Basin mode	IOB	SSTAs averaged over 40°–100°E, 20°S–20°N	(*Xie et al. 2009*)
Indian Ocean Dipole mode	IOD	SSTAs averaged over 50°–70°E, 10°S–10°N minus those averaged over 90°–110°E, 10°S–0°N	(*Saji et al. 1999*)
Southern Indian Ocean Dipole mode	SIOD	SSTAs averaged over 65°–85°E, 25°–10°S minus those averaged over 90°–120°E, 30°–10°S	(*Jo et al. 2022*)
Tropical North Atlantic variability	TNA	SSTAs averaged over 55°–15°W, 5°–25°N	(*Enfield et al. 1999*)
Atlantic Niño	ALT3	SSTAs averaged over 20°W–0°E, 3°S–3°N	(*Nnamchi et al. 2015*)
South Atlantic Subtropical Dipole	SASD	SSTAs averaged over 60°–0°W, 45°–35°S minus those averaged over 40°W–20°E, 30°–20°S	(*Rodrigues et al. 2015*)

Supplementary Table 2. Observational data used in the study.

Dataset (Period)	Variables	Description and Reference	Source
HadISST (1871-2023)	SST	Hadley Centre Sea Ice and Sea Surface Temperature dataset version 1.1 (*Rayner et al. 2003*)	https://www.metoffice.gov.uk/hadobs/hadisst/
ERSSTv5 (1871-2023)	SST	Extended Reconstructed Sea Surface Temperature version 5 (*Huang et al. 2017*)	https://psl.noaa.gov/data/gridded/data.noaa.ersst.v5.html
COBE-SST2 (1871-2023)	SST	Centennial in situ Observation-Based Estimates of Sea Surface Temperature version 2 (*Hirahara et al. 2014*)	https://ds.data.jma.go.jp/tcc/tcc/products/elnino/cobesst_doc.html
GECCO3 (1950-2018)	SST, Temp*	German contribution to Estimating the Circulation and Climate of the Ocean version 3 (*Köhl 2020*)	https://icdc.cen.uni-hamburg.de/thredds/catalog/ftpthredds/EASYInit/GECCO3/regular_1x1_grid/catalog.html
GODAS (1950-2023)	SST, Temp	Global Ocean Data Assimilation System (*Behringer and Xue 2004*)	https://psl.noaa.gov/data/gridded/data.godas.html
ORAS5 (1958-2023)	SST, Temp	ECMWF Ocean Reanalysis System 5 (*Zuo et al. 2019*)	https://doi.org/10.24381/cds.67e8eeb7
ORA20C (1900-2009)	SST, Temp	ECMWF Ocean Reanalysis of the 20th Century (*de Boisséson et al. 2018*)	https://www.cen.uni-hamburg.de/en/icdc/data/ocean/easy-init-ocean/ecmwf-ensemble-of-ocean-reanalyses-of-the-20th-century-ora-20c.html
PEODAS (1960-2014)	SST, Temp	Predictive Ocean Atmosphere Model for Australia Ensemble Ocean Data Assimilation System (*Yin et al. 2011*)	http://opendap.bom.gov.au:8080/thredds/catalogs/bmrc-poama-catalog.html
SODA224 (1871-2010)	SST, Temp	Simple Ocean Data Assimilation Phase 2.2.4 (*Carton and Giese 2008*)	https://apdrc.soest.hawaii.edu/dods/public_data/SODA
ERA5 (1979-2022)	Surface air temperature	ECMWF Atmospheric Reanalysis v5 (*Hersbach et al. 2020*)	https://doi.org/10.24381/cds.f17050d7
CMAP (1979-2022)	Precipitation	Gridded precipitation from the Climate Prediction Center Merged Analysis of Precipitation (*Xie and Arkin 1997*)	https://psl.noaa.gov/data/gridded/data.cmap.html

*Temp is 3-dimensional ocean temperature

Supplementary Table 3. El Niño type forecasts for the Nov-Dec-Jan target season, based on Niño3 and Niño4 indices at a 9-month lead-time.

Year	ORAS5	XRO2 fitted on 1979-2022 (lead=9)	XRO2 fitted on 1950-1990 (lead=9)	AI (lead=9)	NMME (lead=9)
1982	EP	EP	-	-	MIX
1986	MIX	MIX	-	MIX	MIX
1991	MIX	MIX	MIX	MIX	MIX
1997	EP	EP	EP	MIX	MIX
2002	MIX	MIX	MIX	Neutral state	MIX
2009	MIX	EP	Neutral state	MIX	MIX
2015	MIX	MIX	MIX	MIX	MIX

Supplementary Table 4. Details of the NMME models used in this study.

Model	Name used here	Period	Ensemble size	Maximum lead time (months)
CMC1-CanCM3	CanCM3	January 1981–December 2019	10	11
CMC2-CanCM4	CanCM4	January 1981–December 2019	10	11
COLA-RSMAS-CCSM4	CCSM4	January 1982–December 2017	10	11
NCEP-CFSv2	CFSv2	January 1982–July 2022	24	9
GEM-NEMO	GEM-NEMO	January 1981–December 2020	10	11
GFDL-CM2p1-aer04	GFDL	January 1982–December 2021	10	11
GFDL-CM2p5-FLOR-A06	GFDL-FLOR	March 1980–December 2021	12	11
GFDL-CM2p5-FLOR-B01	GFDL-FLOR	March 1980–December 2021	12	11
GFDL-SPEAR	GFDL-SPEAR	January 1991–December 2020	15	11
NASA-GEOSS2S	NASA-GEOSS2S	January 1981–December 2020	10	8

Supplementary Table 5. Lists of the 91 CMIP5/6 climate models used in this study.

CMIP5 No.	CMIP5 Models	Member	CMIP6 No.	CMIP6 Models	Member
1	ACCESS1-0	r1i1p1	1	ACCESS-CM2	r1i1p1f1
2	ACCESS1-3	r1i1p1	2	ACCESS-ESM1-5	r1i1p1f1
3	bcc-csm1-1	r1i1p1	3	AWI-CM-1-1-MR	r1i1p1f1
4	bcc-csm1-1-m	r1i1p1	4	BCC-CSM2-MR	r1i1p1f1
5	BNU-ESM	r1i1p1	5	BCC-ESM1	r1i1p1f1
6	CanESM2	r1i1p1	6	CAMS-CSM1-0	r1i1p1f1
7	CCSM4	r1i1p1	7	CAS-ESM2-0	r1i1p1f1
8	CESM1-BGC	r1i1p1	8	CESM2	r4i1p1f1
9	CESM1-CAM5	r1i1p1	9	CESM2-FV2	r1i1p1f1
10	CESM1-FASTCHEM	r1i1p1	10	CESM2-WACCM	r1i1p1f1
11	CESM1-WACCM	r1i1p1	11	CESM2-WACCM-FV2	r1i1p1f1
12	CMCC-CESM	r1i1p1	12	CIESM	r1i1p1f1
13	CMCC-CM	r1i1p1	13	CMCC-CM2-HR4	r1i1p1f1
14	CMCC-CMS	r1i1p1	14	CMCC-CM2-SR5	r1i1p1f1
15	CNRM-CM5	r1i1p1	15	CMCC-ESM2	r1i1p1f1
16	CSIRO-Mk3-6-0	r1i1p1	16	CNRM-CM6-1	r1i1p1f2
17	FGOALS-g2	r1i1p1	17	CNRM-ESM2-1	r1i1p1f2
18	FGOALS-s2	r1i1p1	18	CanESM5	r1i1p1f1
19	FIO-ESM	r1i1p1	19	E3SM-1-0	r1i1p1f1
20	GFDL-CM3	r1i1p1	20	E3SM-1-1	r1i1p1f1
21	GFDL-ESM2G	r1i1p1	21	E3SM-1-1-ECA	r1i1p1f1
22	GFDL-ESM2M	r1i1p1	22	EC-Earth3	r1i1p1f1
23	GISS-E2-H-CC	r1i1p1	23	EC-Earth3-Veg	r1i1p1f1
24	GISS-E2-H	r1i1p1	24	FGOALS-f3-L	r1i1p1f1
25	GISS-E2-R-CC	r1i1p1	25	FGOALS-g3	r1i1p1f1
26	GISS-E2-R	r1i1p1	26	FIO-ESM-2-0	r1i1p1f1
27	HadCM3	r1i1p1	27	GFDL-CM4	r1i1p1f1
28	HadGEM2-AO	r1i1p1	28	GFDL-ESM4	r1i1p1f1
29	HadGEM2-CC	r1i1p1	29	GISS-E2-1-G	r1i1p1f1
30	HadGEM2-ES	r1i1p1	30	GISS-E2-1-G-CC	r1i1p1f1
31	IPSL-CM5A-LR	r1i1p1	31	GISS-E2-1-H	r1i1p1f1
32	IPSL-CM5A-MR	r1i1p1	32	HadGEM3-GC31-LL	r1i1p1f3
33	IPSL-CM5B-LR	r1i1p1	33	INM-CM4-8	r1i1p1f1
34	MIROC5	r1i1p1	34	INM-CM5-0	r10i1p1f1
35	MIROC-ESM-CHEM	r1i1p1	35	IPSL-CM6A-LR	r1i1p1f1
36	MIROC-ESM	r1i1p1	36	MIROC6	r1i1p1f1
37	MPI-ESM-LR	r1i1p1	37	MIROC-ES2L	r1i1p1f2
38	MPI-ESM-MR	r1i1p1	38	MPI-ESM-1-2-HAM	r1i1p1f1
39	MPI-ESM-P	r1i1p1	39	MPI-ESM1-2-HR	r1i1p1f1
40	MRI-CGCM3	r1i1p1	40	MPI-ESM1-2-LR	r10i1p1f1
41	MRI-ESM1	r1i1p1	41	MRI-ESM2-0	r1i2p1f1
42	NorESM1-ME	r1i1p1	42	NESM3	r1i1p1f1
43	NorESM1-M	r1i1p1	43	NorESM2-LM	r1i1p1f1
			44	NorESM2-MM	r1i1p1f1
			45	SAM0-UNICON	r1i1p1f1
			46	TaiESM1	r1i1p1f1
			47	UKESM1-0-LL	r1i1p1f2
			48	NorCPM1	r1i1p1f1

Supplementary Figures

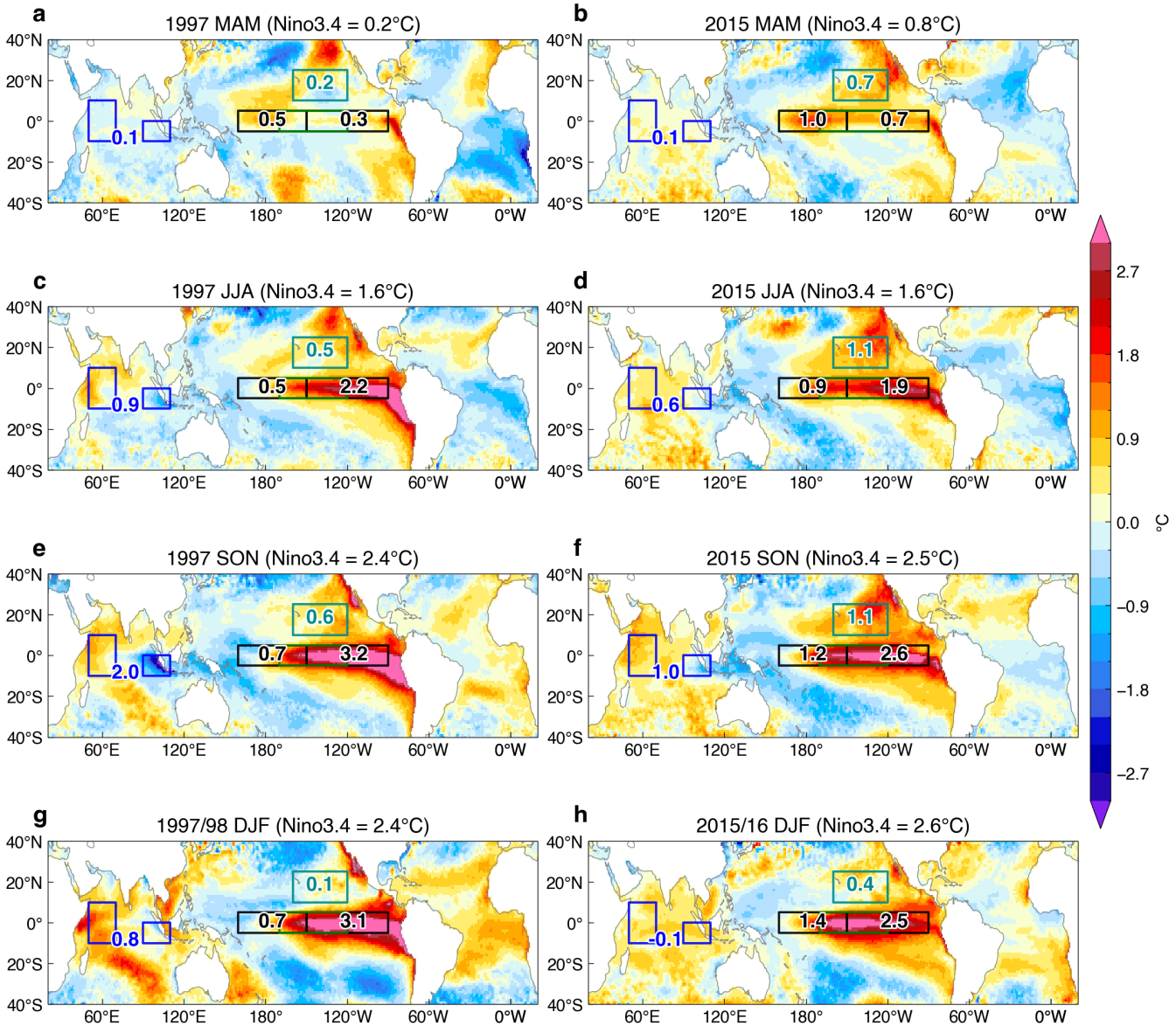

Supplementary Fig. 1| Observed differences in tropical SSTA pattern and evolution between the 1997/98 and 2015/16 El Niño events derived from ORAS5 reanalysis. The SSTAs during (a) 1997 MAM, (b) 2015 MAM, (c) 1997 JJA, (d) 2015 JJA, (e) 1997 SON, (f) 2015 SON, (g) 1997/98 DJF and (h) 2015/16 DJF. In each panel, the values of Niño3, Niño4, IOD, and NPMM SSTAs are indicated in the corresponding boxes, and the value of Niño3.4 is indicated in the title. The 1997/98 and 2015/16 El Niño events have different SSTA patterns in the central and far eastern equatorial Pacific, as well as different associated IOD and NPMM intensities. The 1997 event exhibits eastern Pacific El Niño characteristics with the warmest SSTAs in the far eastern equatorial Pacific and a strong concurrent IOD, partly due to stronger WWV preconditioning. In 2015, the SSTA peak is located closer to the central Pacific, possibly due to the strong coupling of the NPMM and central equatorial Pacific SST.

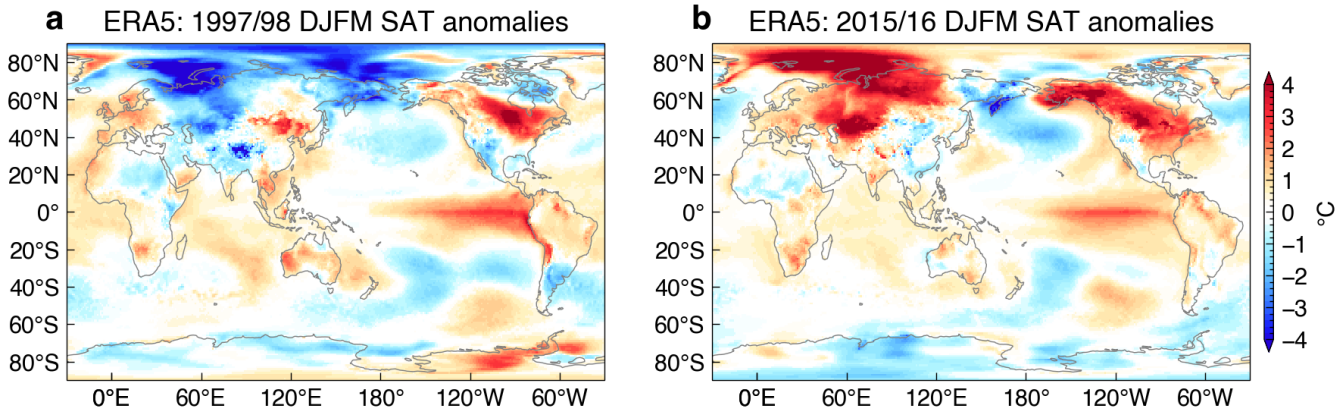

Supplementary Fig. 2| Observed surface air temperature (SAT) anomalies for the 1997/98 and 2015/16 El Niño events during December-March (DJFM). The (a) 1997/98 and (b) 2015/16 El Niño events were associated with different pan-Arctic SAT, consistent with Jeong et al. (*2022*).

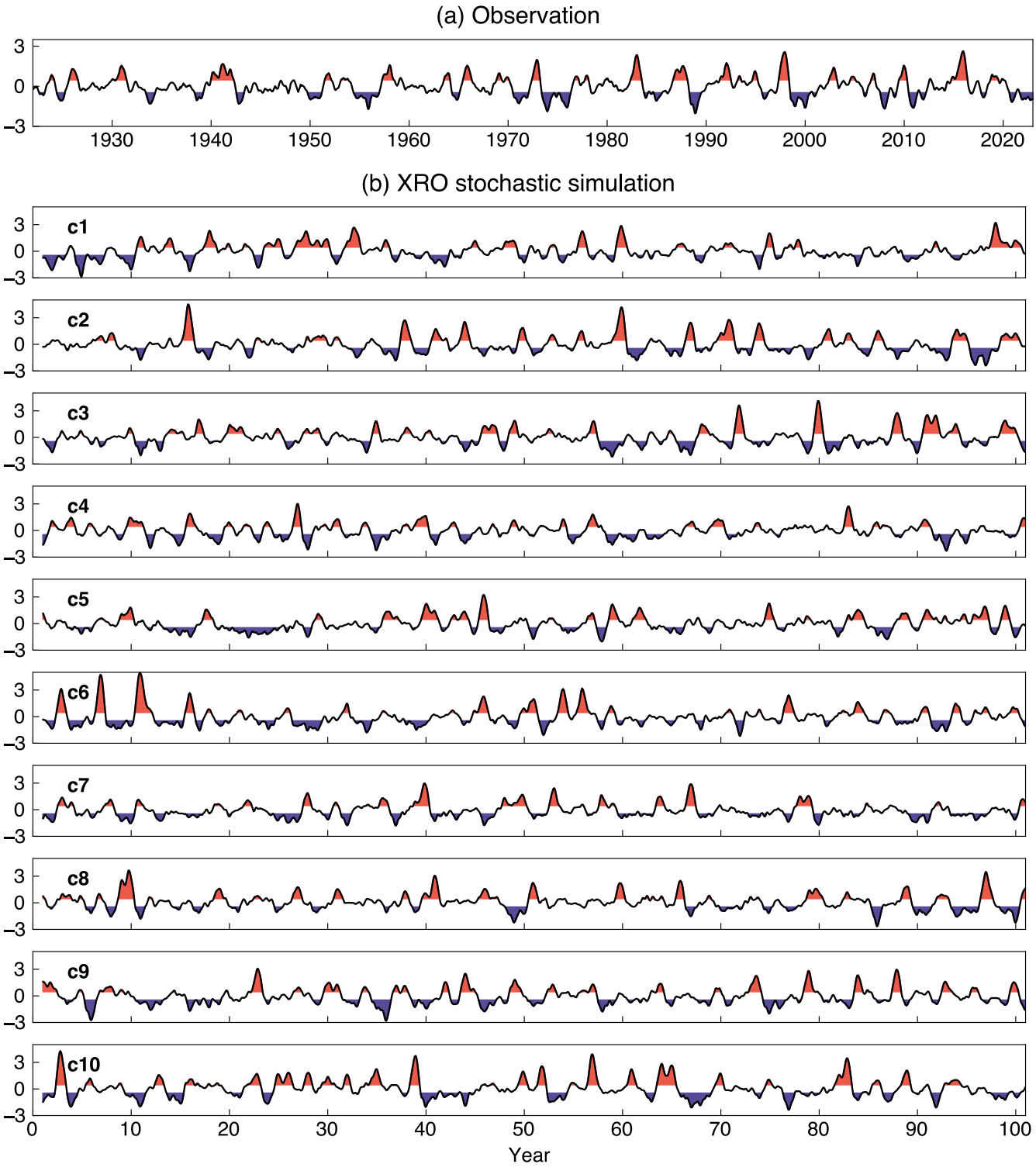

Supplementary Fig. 3| ENSO time series in the observation and XRO stochastic simulation. The 3-month running mean of Niño3.4 SSTA for (**a**) the ensemble mean of multiple observational SST datasets for 1923-2022 (Supplementary Table 2), and (**b**) the 10 consecutive centuries (numbered) from the XRO stochastic simulation. The red/blue shading denote the SSTA above 0.5 / below -0.5℃, respectively. The XRO stochastic simulation reproduces the irregular interannual oscillations between El Niño and La Niña.

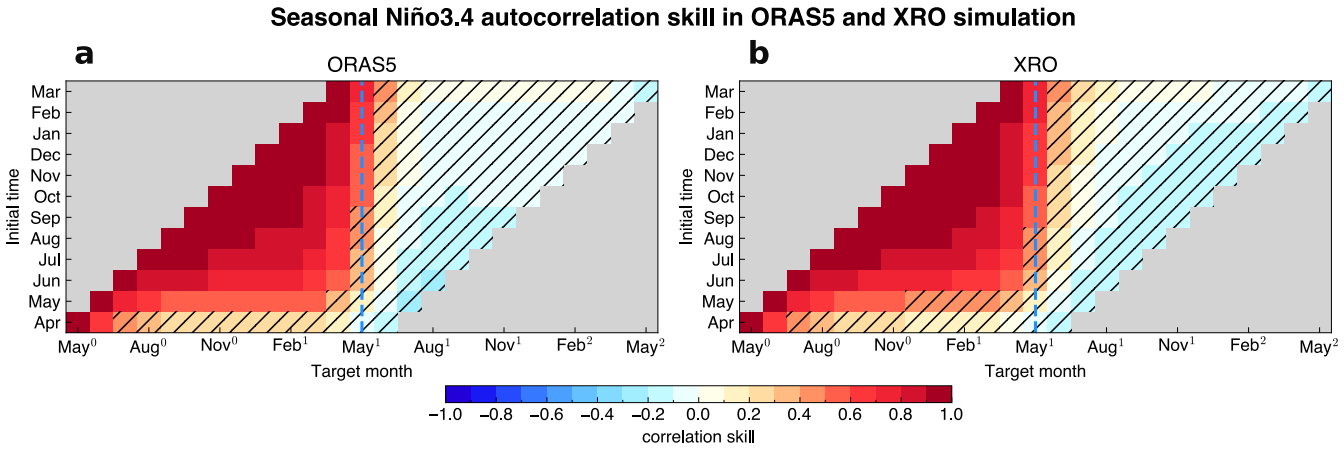

Supplementary Fig. 4| Seasonal autocorrelation of Niño3.4 SST index. Correlations of Niño3.4 index with itself, as a function of initialization month (ordinate) and target month (abscissa) for the ORAS5 reanalysis (1979-2022) (**a**) and for the XRO stochastic simulations (**b**, ensemble mean). Hatching highlights correlation skills less than 0.5. The dashed vertical blue lines denote the spring predictability barrier season. The XRO accurately reproduces the rapid decline in ENSO SSTA autocorrelation across boreal spring.

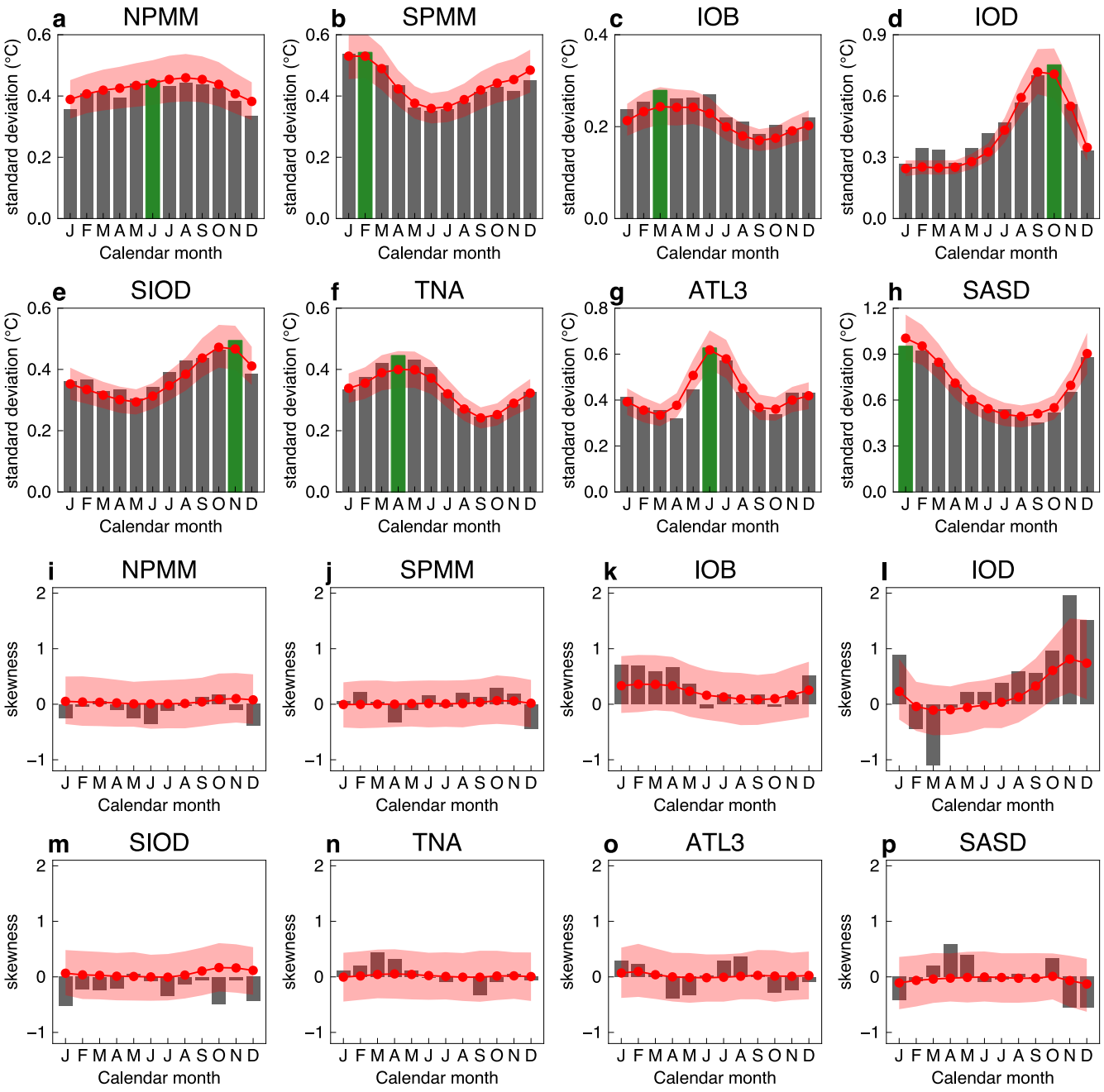

Supplementary Fig. 5| Seasonal statistics of SSTA indices for the other climate modes. a-h, Seasonally varying standard deviation of the SSTA indices for the NPMM, SPMM, IOB, IOD, SIOD, TNA, ATL3, and SASD, respectively, in the ORAS5 observations (1979-2022) (*bars*) and the XRO stochastic simulations (*red curves*). Red shading indicates the 10%-90% spread bands of simulated 43-year epochs, obtained from splitting a 43,000-year XRO simulation into 1000 non-overlapping blocks. The month of peak standard deviation for each observed mode is indicated in green. **i-p**, Same as a-h, but for seasonally varying skewness. The XRO accurately simulates the observed seasonal synchronization of specific climate modes, and reasonably reproduces the observed warm/cold asymmetries of both the IOB and IOD.

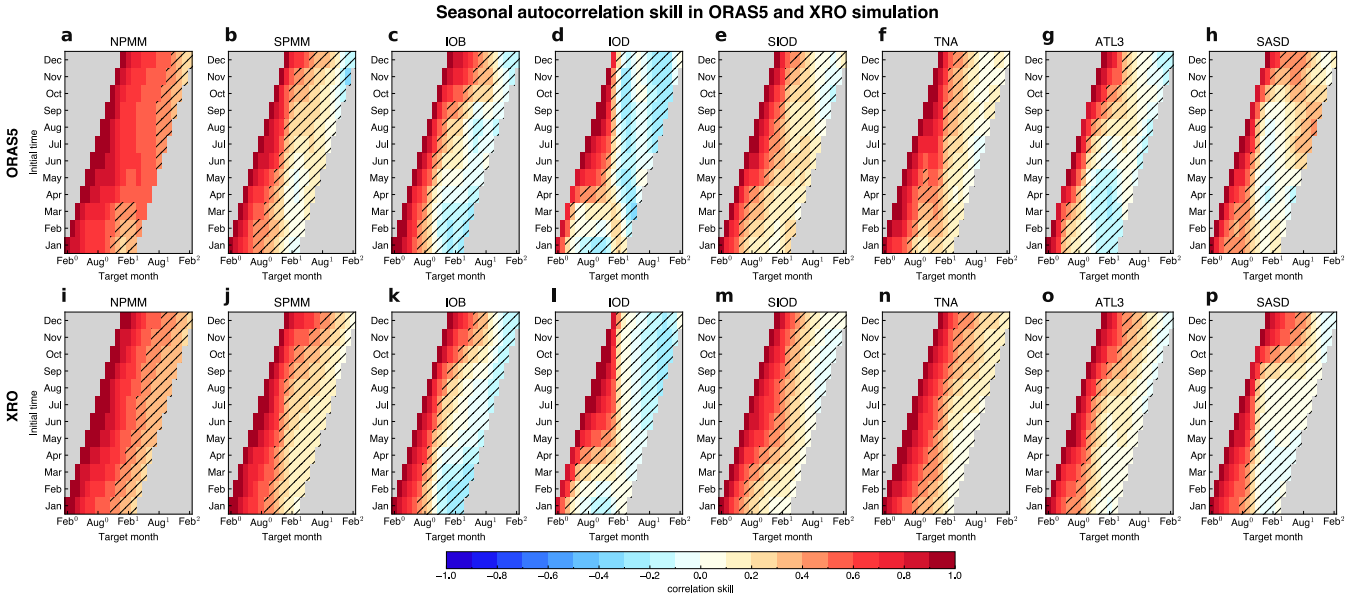

Supplementary Fig. 6| Seasonal autocorrelation of SSTA indices for other climate modes. Correlations of each index with itself, as a function of initialization month (ordinate) and target month (abscissa) for the ORAS5 reanalysis (1979-2022) (upper row) and for the XRO stochastic simulations (bottom row, ensemble mean). Hatching highlights correlation skills less than 0.5. The XRO accurately reproduces the seasonal autocorrelation structures of the other climate modes.

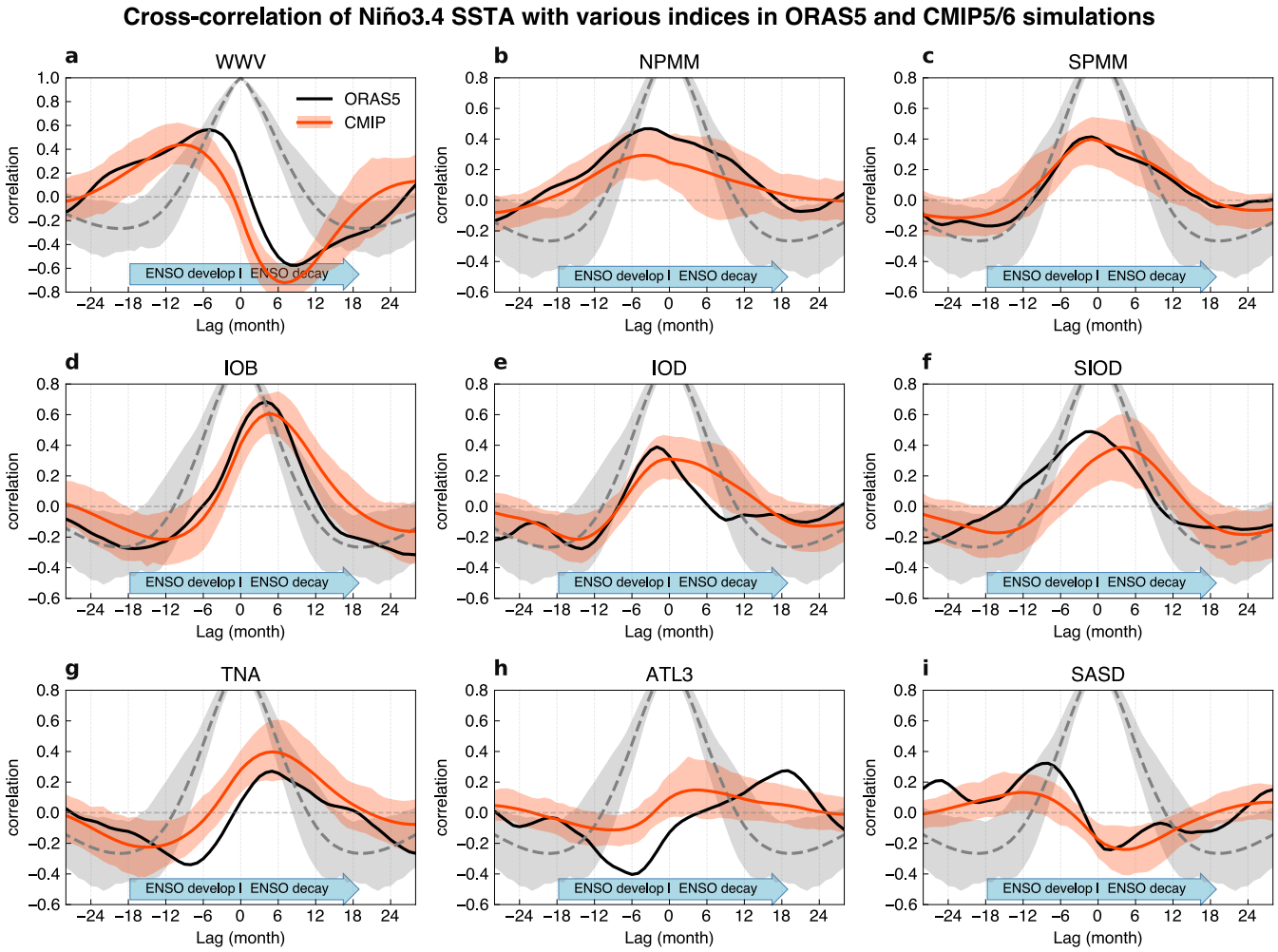

Supplementary Fig. 7| ENSO's lead-lag relationship with equatorial Pacific warm water volume (WWV) index and SSTA indices of other climate modes in CMIP historical simulations. Shown as monthly cross-correlations of each index with the lagged Niño3.4 index in ORAS5 reanalysis (1979-2022) (*black*) and CMIP5/6 historical simulations (1900-1999) (ensemble mean in red curves; red shading indicates the 10%-90% spread bands of 91 individual models). The dashed curves show the ensemble mean autocorrelation of Niño3.4 index in CMIP5/6 historical simulations (shading indicates the 10%-90% spread bands of 91 individual models). Abscissas are the lead-time, with negative values representing months for which the Niño3.4 index lags, and positive values representing months for which the Niño3.4 index leads. It is challenging for climate models to realistically simulates the observed ENSO SSTA lead-lag relationship with WWV anomalies and the SSTA indices for the other climate modes, especially for WWV index and Atlantic Ocean SST indices.

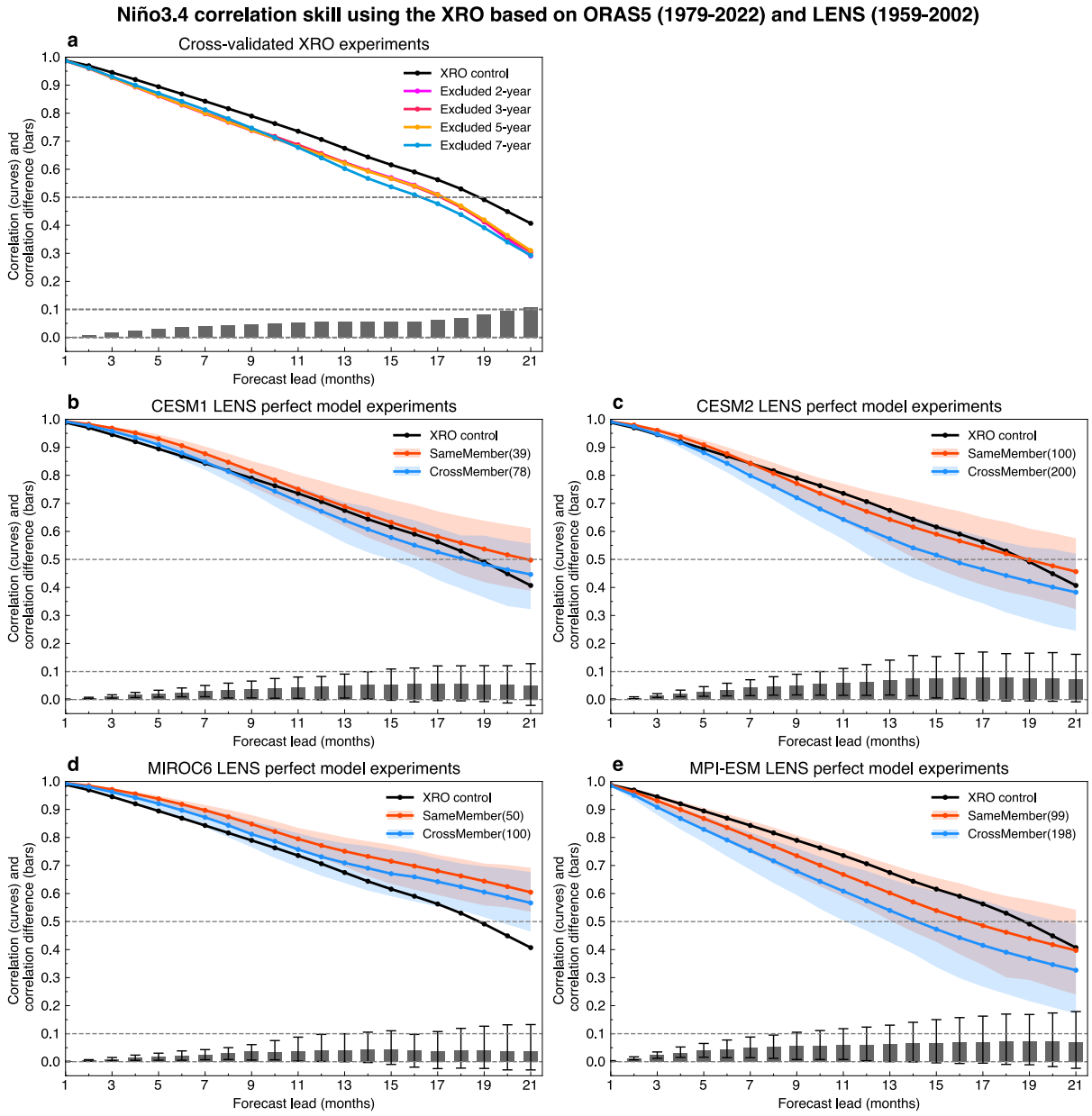

Supplementary Fig. 8| Robustness of the XRO parameter fitting and reforecasting ENSO. **a**, the all-months correlation skill of the 3-month running mean Niño3.4 index during 1979-2022 as a function of forecast lead for the XRO control forecast (*black curve*) and cross-validated XRO forecast that excluded from 2 to 7 years data (*coloured curves*), the mean skill difference between cross-validated XRO forecast and control forecast (*bars*). The dashed lines indicate 0.5, 0.1, and zero correlation skills. **b-d**, Same as **a**, but for skill for LENS perfect model "Same-Member" and "Cross-Member" experiments for CESM1, CESM2, MIROC6, and MPI-ESM during 1959-2002, respectively (See *"Large ensemble simulations and perfect model reforecasting experiments" in Methods*). The shadings denote the 10%-90% spread among the ensemble members within each LENS. The bottom bars denote the mean difference between "Same-Member" and "Cross-Member" experiments with error bars denote the 10%-90% spread among the ensemble members within each LENS. The XRO fitting and reforested ENSO is robust with uncertainty in Niño3.4 correlation skill less than 0.1 within 21 lead months.

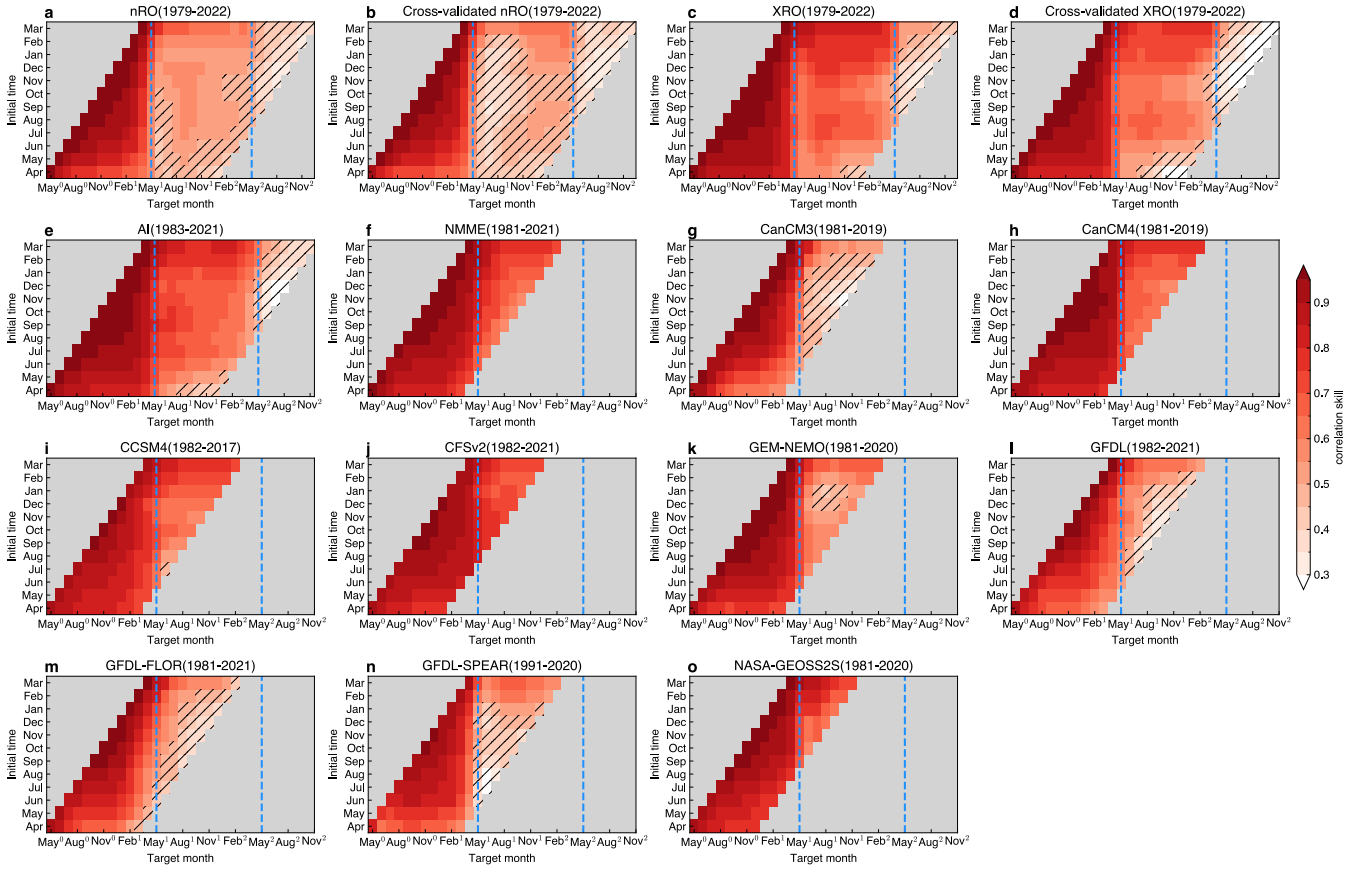

Supplementary Fig. 9| Seasonality of correlation forecast skill for ENSO. The correlation skills verified during 1979-2022 of various model forecasts of the Niño3.4 SSTA index, as a function of the start month (ordinate) and target month (abscissa; superscripts 0, 1, 2 denote the current and subsequent years, respectively), for the nRO (a), Cross-validated nRO (b), XRO (c), Cross-validated XRO (d), AI model (e), multi-model mean of NMME ensemble means (f), and ensemble means from individual dynamical models in the North American Multi-Model Ensemble (NMME)(g-o). Hatching highlights the forecasts with correlation skill less than 0.5. The dashed vertical blue lines denote the spring predictability barrier season. The nRO and most of the dynamical models exhibit a pronounced spring predictability barrier in May-June-July. The SPB is much less pronounced in the XRO, which is comparable in skill with the AI model in all seasons.

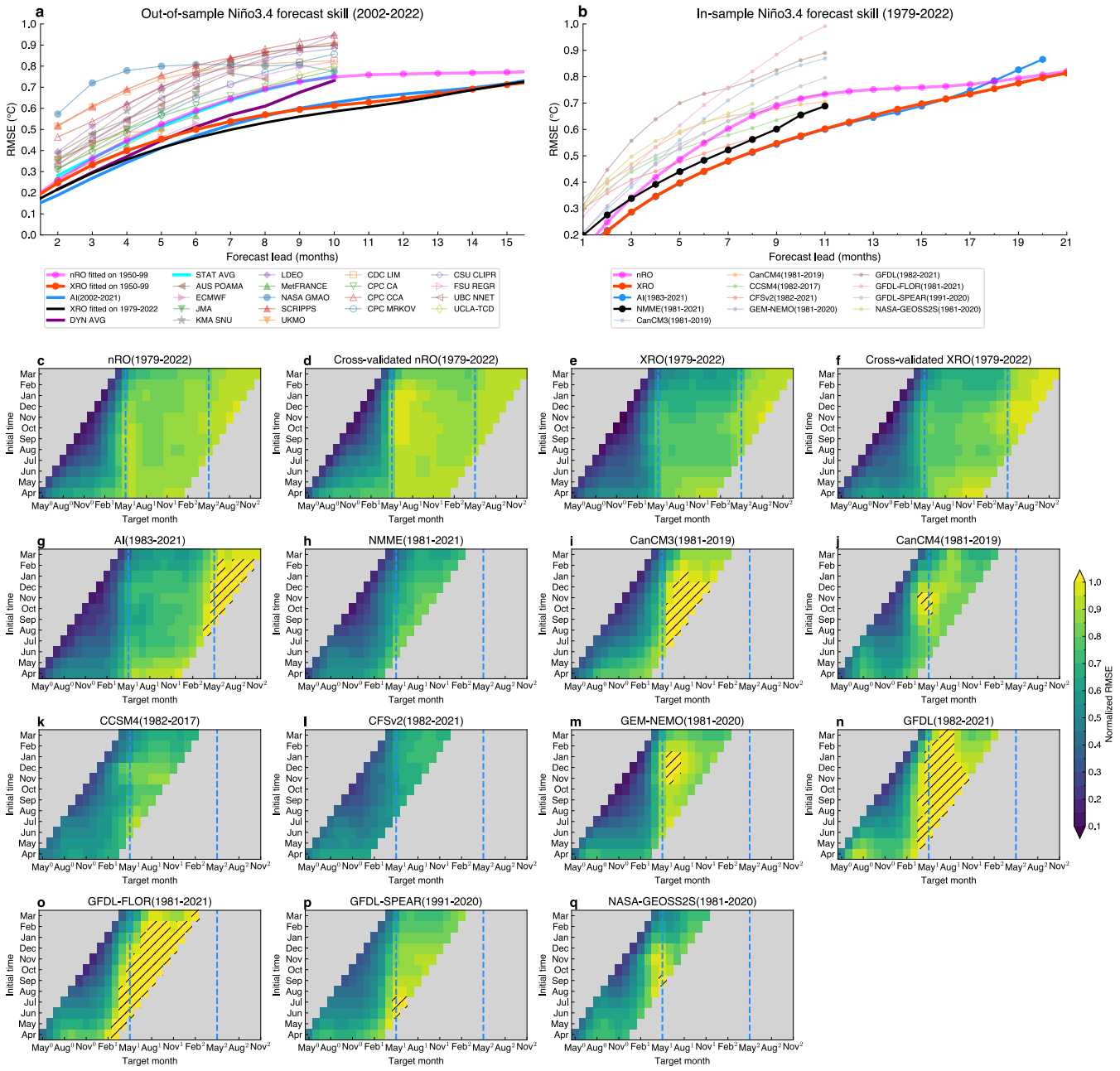

Supplementary Fig. 10| Root Mean Square Error (RMSE) forecast metric for ENSO. **a**, The all-months RMSE forecasts verified on 2002-2022 of the 3-month running mean Niño3.4 SSTA index, as a function of the forecast lead month in the out-of-sample nRO fitted on 1950-1999 (*magenta*), out-of-sample XRO fitted on 1950-1999 (*red*), the AI model, the XRO control fitted on 1979-2022 (*black curve*) and operational models aggregated by the International Research Institute for Climate and Society (IRI), ensemble mean of dynamical models (DYN AVG, *dark purple curve*), ensemble mean of statistical models (STAT AVG, *dark cyan curve*). **b**, same as **a**, but for RMSE skill of Niño3.4 forecasts verified 1979-2022 in the in-sample nRO (*magenta*), in-sample XRO model (*red*), AI model (*blue*), dynamical models from the North American Multi-Model Ensemble (NMME) project (multi-model ensemble of NMME in *black*, ensemble mean from individual models in *other colours*); **c-q**, The relative RMSE of

Niño3.4 SSTA forecasts, normalized by the seasonally-varying standard deviation of the observations, as a function of the forecast start month (ordinate) and target month (abscissa; superscripts 0, 1, 2 denote the current and subsequent years, respectively), for the nRO, cross-validated nRO, XRO, cross-validated XRO, AI model, dynamical models from the North American Multi-Model Ensemble (NMME) project (multi-model ensemble of NMME, ensemble mean from individual models). The dashed vertical blue lines denote the spring predictability barrier season. The superior efficacy of the XRO in ENSO forecasting is supported by the RMSE metric.

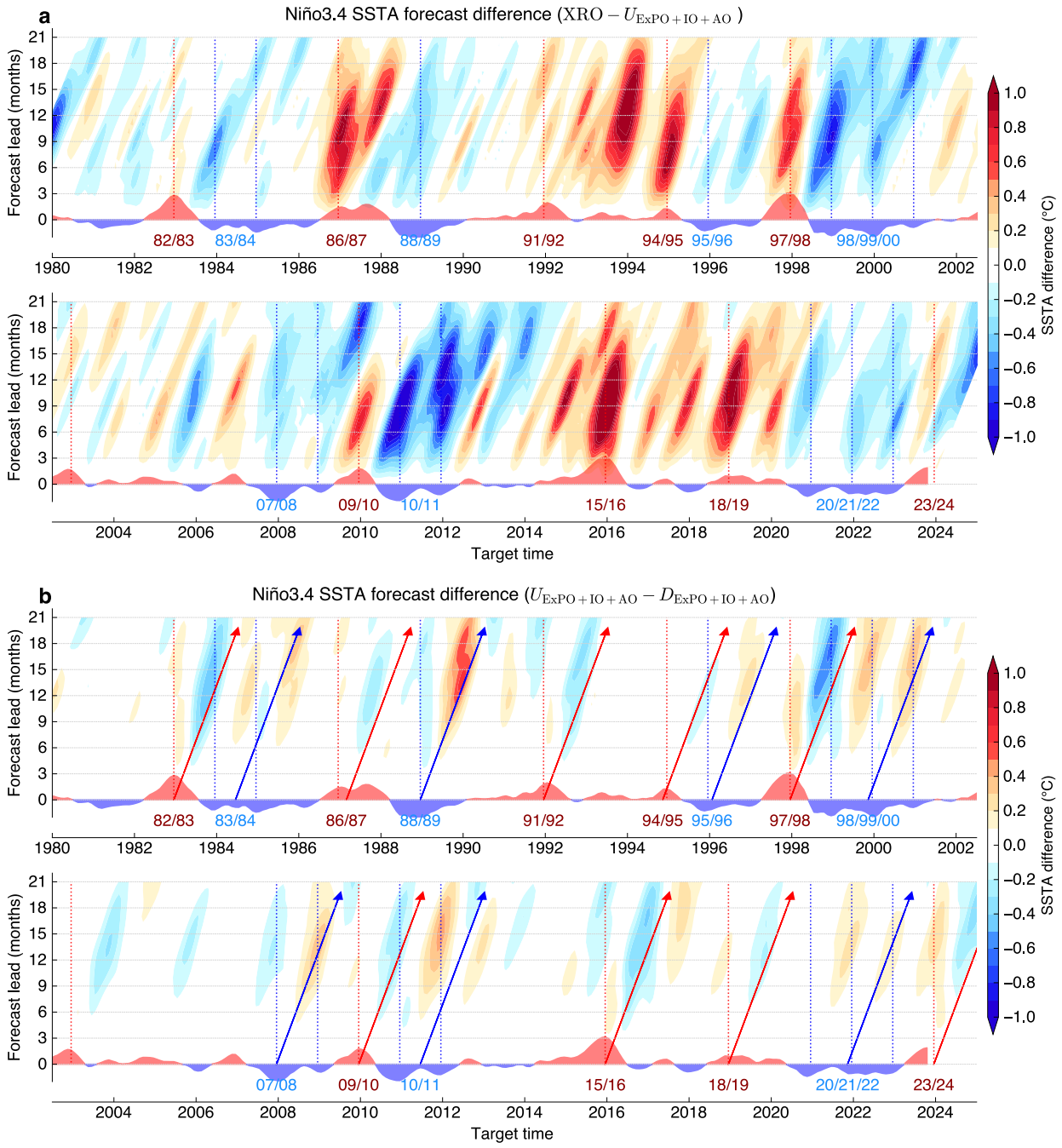

Supplementary Fig. 11| Comparison role of climate-mode interactions on Niño3.4 forecast between the component due to other climate modes' initial state and the component due to the ENSO initial state. Shown are the differences of Niño3.4 SSTA (*shading*) as a function of forecast lead and target time between the control and uninitialized ExPO+IO+AO experiment (a), and between the uninitialized ExPO+IO+AO and decoupled ExPO+IO+AO experiment forecasts (b). Vertical reference dashed lines denote December of El Niño (red) and La Niña (blue) years, respectively. The observed normalized time series of Niño3.4 SSTA index is indicated in the bottom axis. In b, the arrows indicate the flow of forecast integration started from the selected time. The other climate modes mainly affect ENSO via their initial condition memory.

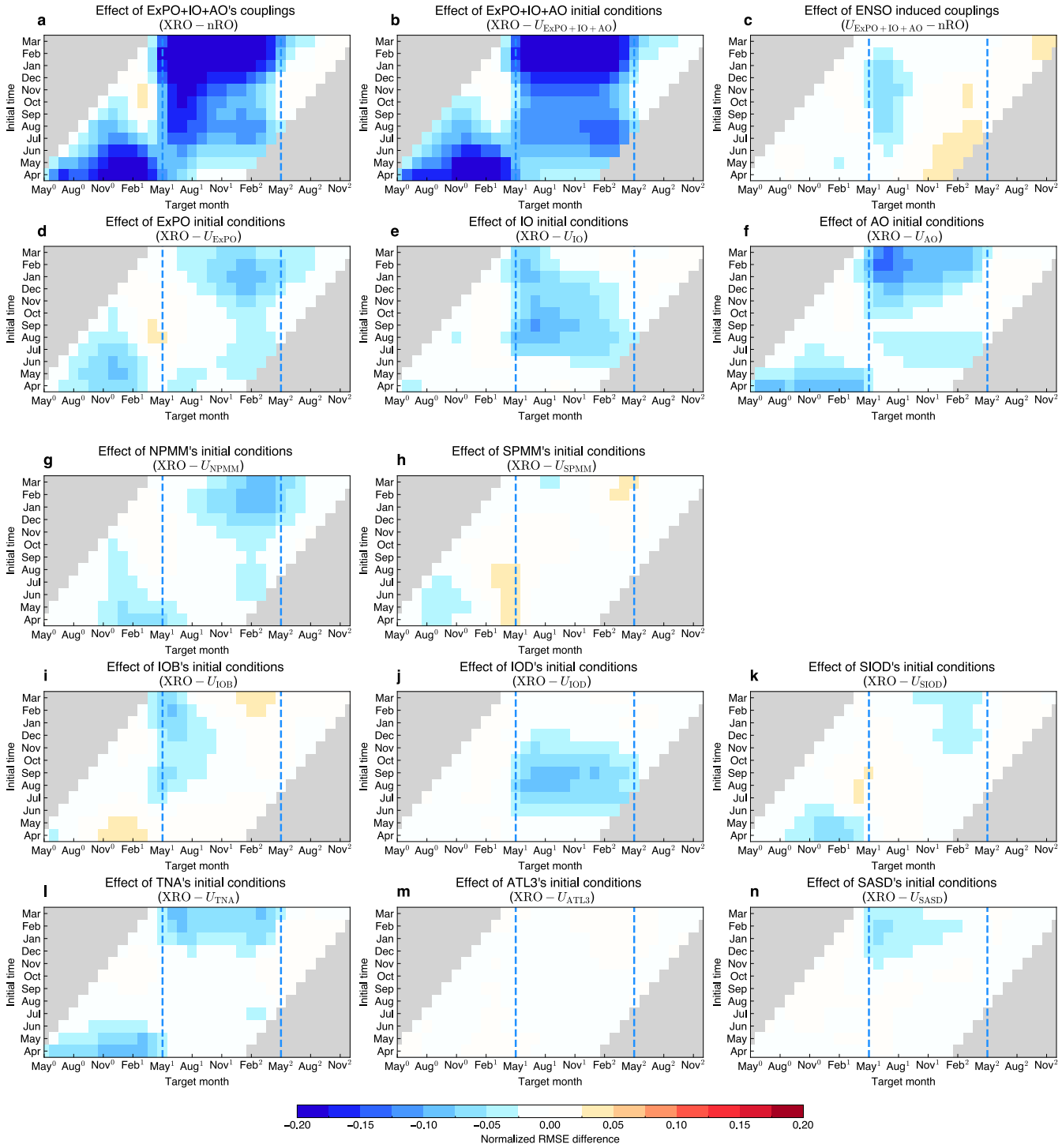

Supplementary Fig. 12| Quantifying the reduced ENSO forecast Root Mean Square Error (RMSE) from the coupled influences outside equatorial Pacific during 1979-2022. Shown is the relative RMSE difference of the Niño3.4 SSTA forecasts, normalized by the seasonally-varying standard deviation of the observations, as a function of the forecast start month (ordinate) and target month (abscissa; superscripts 0, 1, 2 denote the current and subsequent years, respectively). **a-d,** the skill difference between XRO and $D_{\mathrm{ExPO+IO+AO}}$ (a), between XRO and $U_{\mathrm{ExPO+IO+AO}}$ (b), and between $U_{\mathrm{ExPO+IO+AO}}$ and $D_{\mathrm{ExPO+IO+AO}}$ (c); **e-n,** the skill difference between control and the uninitialized ExPO, IO, AO, NPMM, SPMM, IOB, IOD,

SIOD, TNA, ATL3, and SASD experiments, respectively. The importance of climate mode interactions in ENSO forecasting is supported by the RMSE metric.

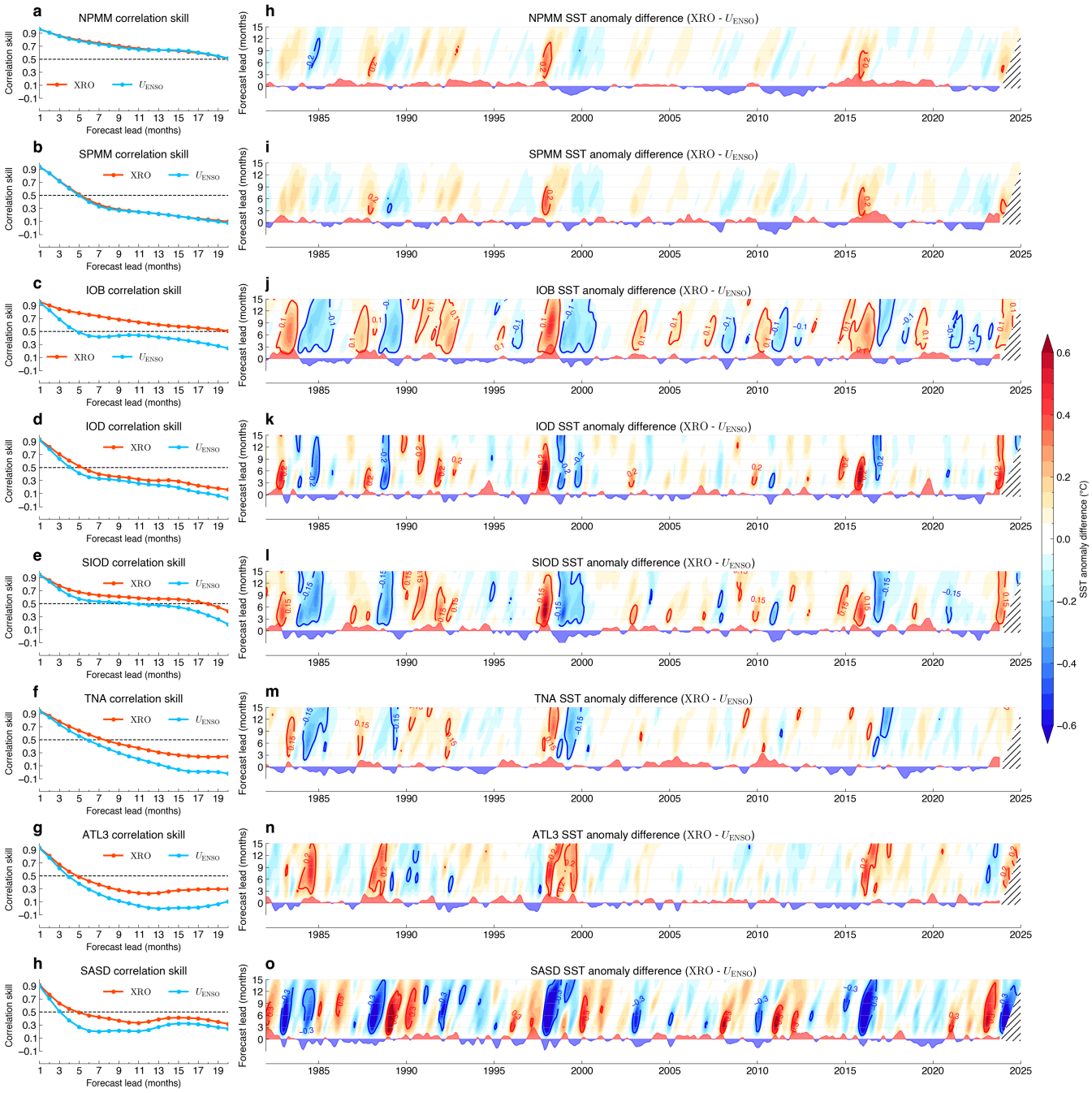

Supplementary Fig. 13| Impact of ENSO's initialization to other climate mode forecasts. Left panels (**a-h**) show the all-months correlation skill of the 3-month running mean each climate mode index during 1979-2022 as a function of forecast lead for the XRO control forecast (*red curve*) and uninitialized ENSO experiment (U_{ENSO}) forecast (*blue curve*). Right panels (**h-o**) show the difference of other climate mode SSTA (shading) as a function of forecast lead and target time, between control and uninitialized ENSO experiment (U_{ENSO}). The normalized time series of each climate mode SSTA index is indicated in the bottom axis. The XRO sensitivity experiments quantify how the initial states of ENSO affect the predictability of the other climate modes.

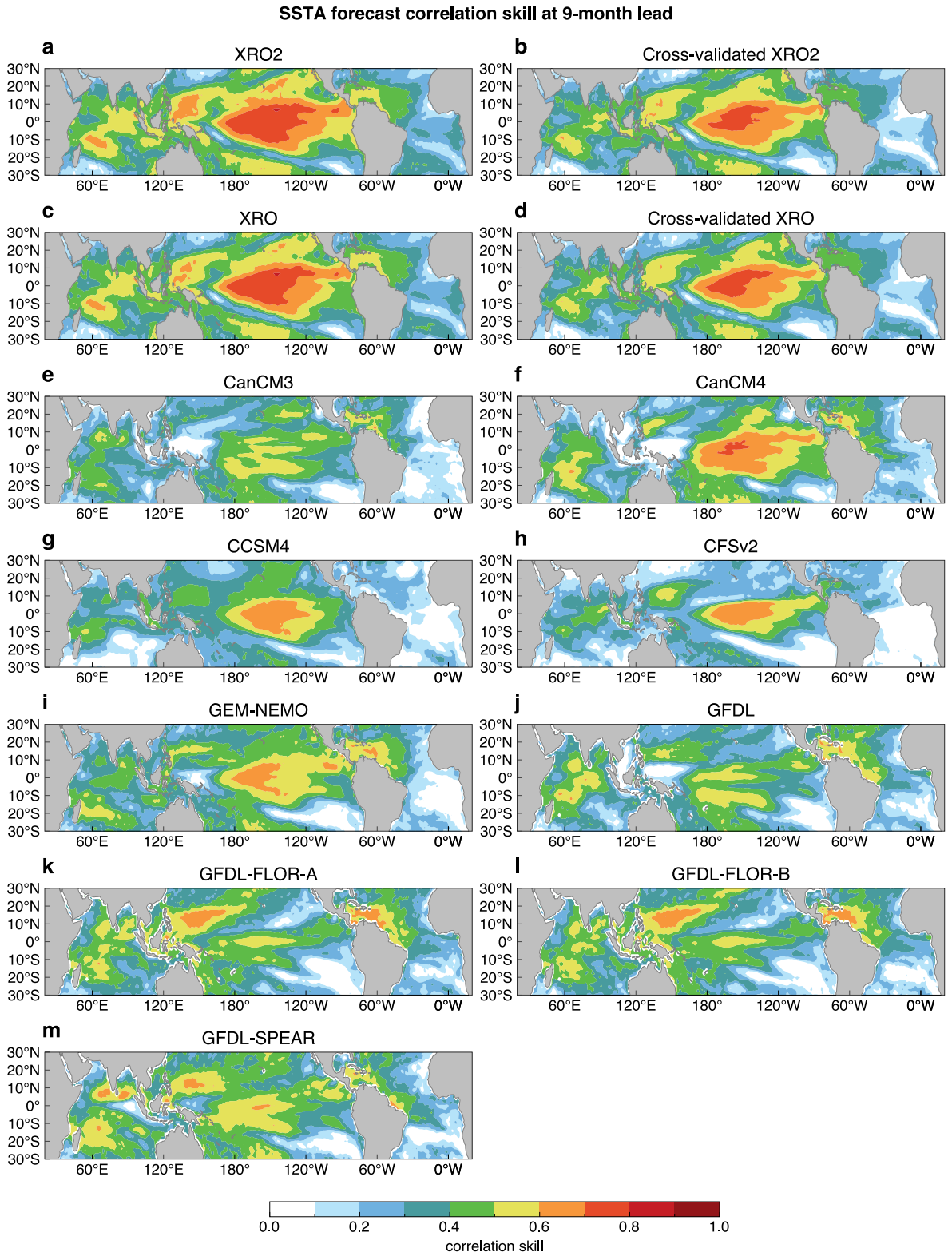
SSTA forecast correlation skill at 9-month lead
a
XRO2
b
Cross-validated XRO2
c
XRO
d
Cross-validated XRO
e
CanCM3
f
CanCM4
g
CCSM4
h
CFSv2
i
GEM-NEMO
j
GFDL
k
GFDL-FLOR-A
l
GFDL-FLOR-B
m
GFDL-SPEAR
30°N
20°N
10°N
0°
10°S
20°S
30°S
60°E
120°E
180°
120°W
60°W
0°W
0.0
0.2
0.4
0.6
0.8
1.0
correlation skill

(*continued*)

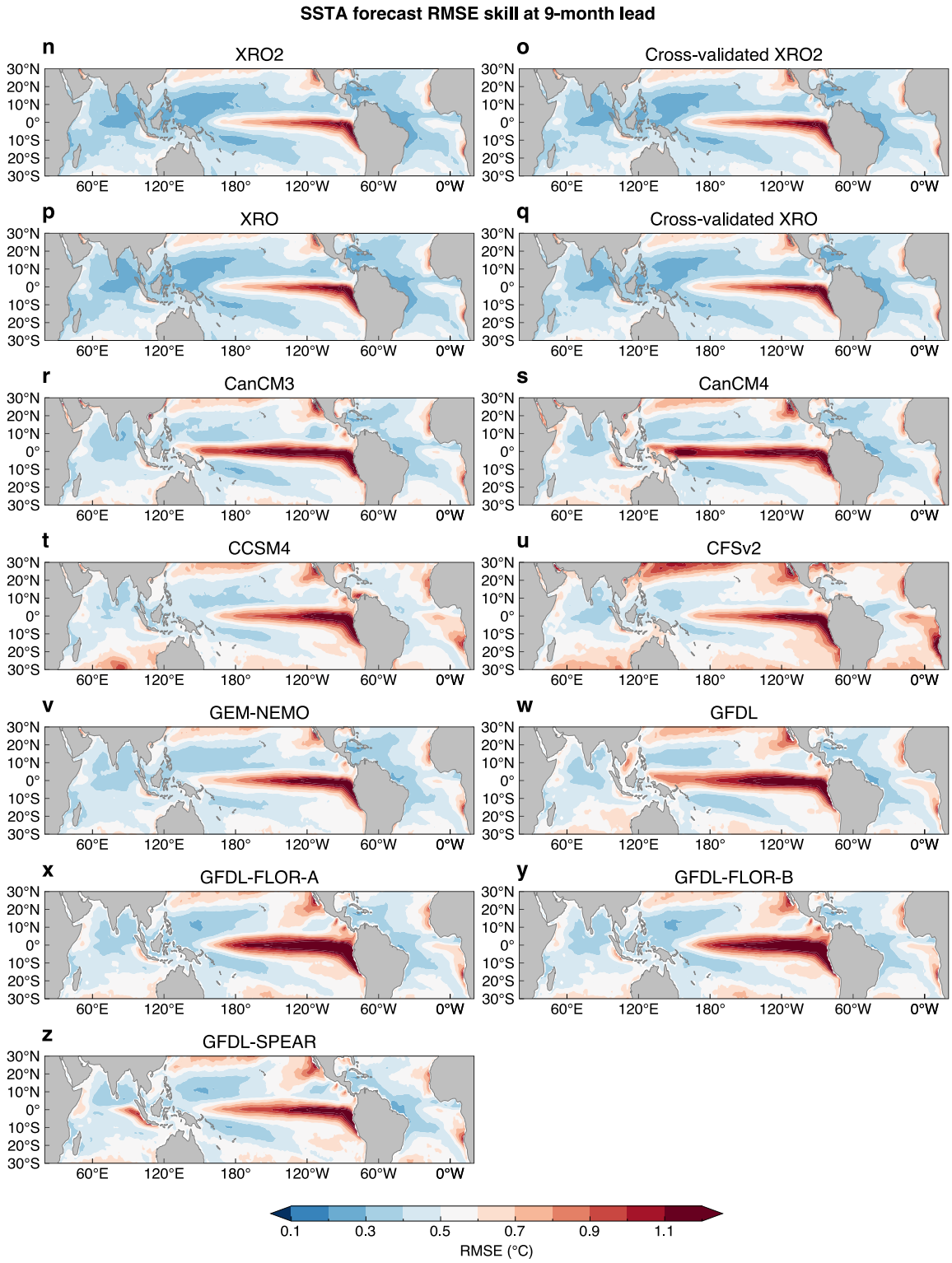

Supplementary Fig. 14| Pantropical SSTA forecast skill at 9-month lead time verified on 1982-2022. Correlation skill (**a-m**) and RMSE (**n-z**) for the SST forecasts include XRO2, cross-validated XRO2, XRO, cross-validated XRO, and the available nine NMME models. The XRO2 provide more skilful SSTA forecast than the operatorial climate models in most of the pantropical regions.

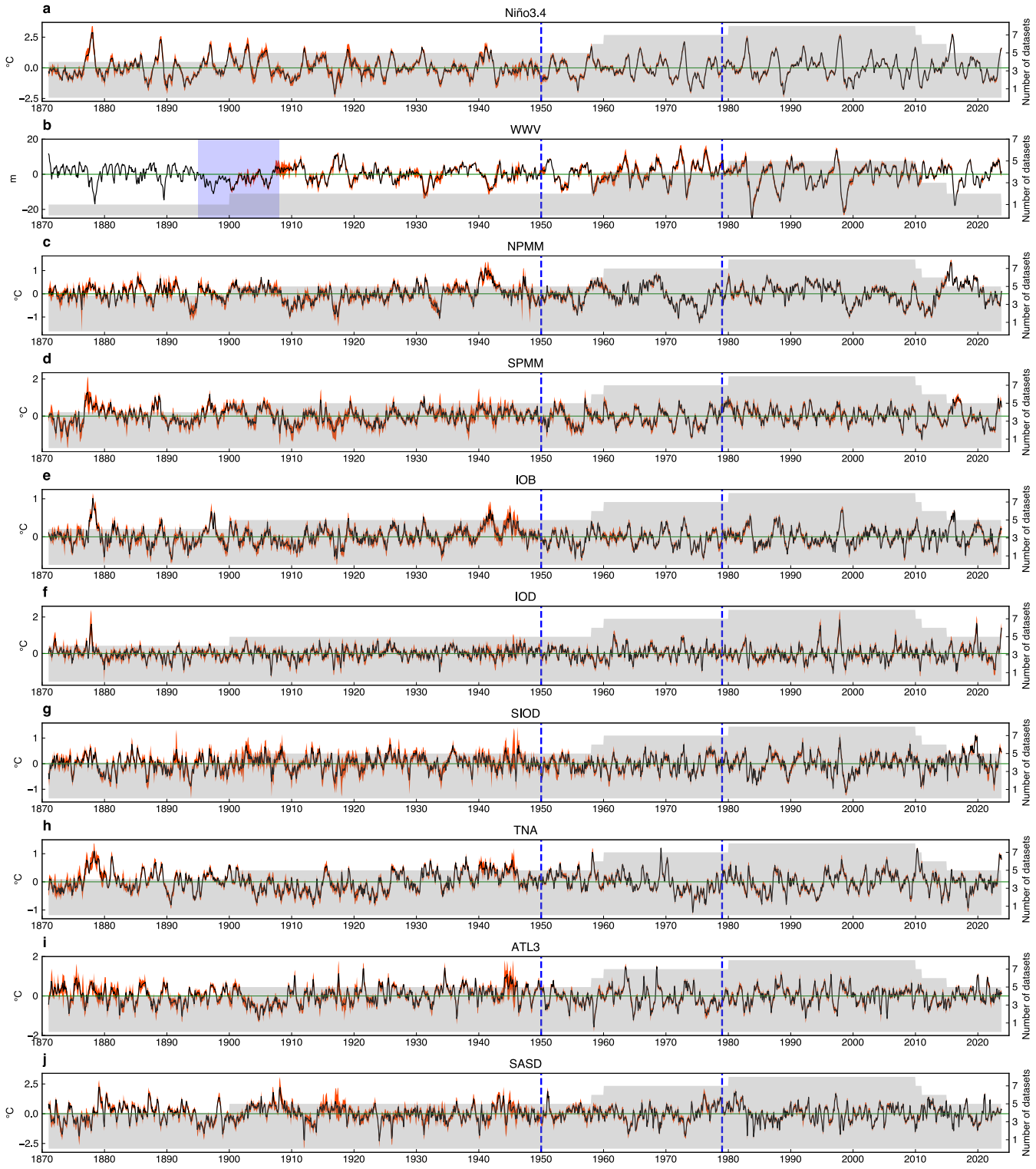

Supplementary Fig. 15| Time series of various SSTA indices and WWV anomaly index in multiple observation/reanalysis datasets. SST datasets include (HadISST: 1871-2023, ERSSTv5: 1871-2023, COBE-SST2: 1871-2023, ORAS5: 1958-2023, SODA224: 1871-2010, ORA20C: 1900-2009, PEODAS: 1960-2014, GECOO3: 1948-2018, GODAS: 1980-2023), WWV datasets include (ORAS5: 1958-2023, SODA224: 1871-2010, ORA20C: 1900-2009, PEODAS: 1960-2014, GECOO3: 1948-2018, GODAS:

1980-2023). The monthly anomalies were calculated by removing the monthly climatology for 1980-2010 and the quadratic trend over the whole period. The black curve is mean of all datasets, the red shading denotes the 10%-90% inter-dataset spread, the grey shading indicates the number of datasets calculated for each month, the blue vertical reference lines denote January of 1950 and 1979. There are large uncertainties in the data before 1950, especially for equatorial Pacific WWV and SSTA in other basins (large inter-dataset spread shown by red shadings), and during time of World War II (1936-1949). There are also periods that are not physically consistent with current theory or understanding of ENSO, for instance, the multiple El Niño events occurred when a long period of discharged WWV state during 1895-1908 (blue shading period, compare with the Nino34 SSTA and WWV anomaly).

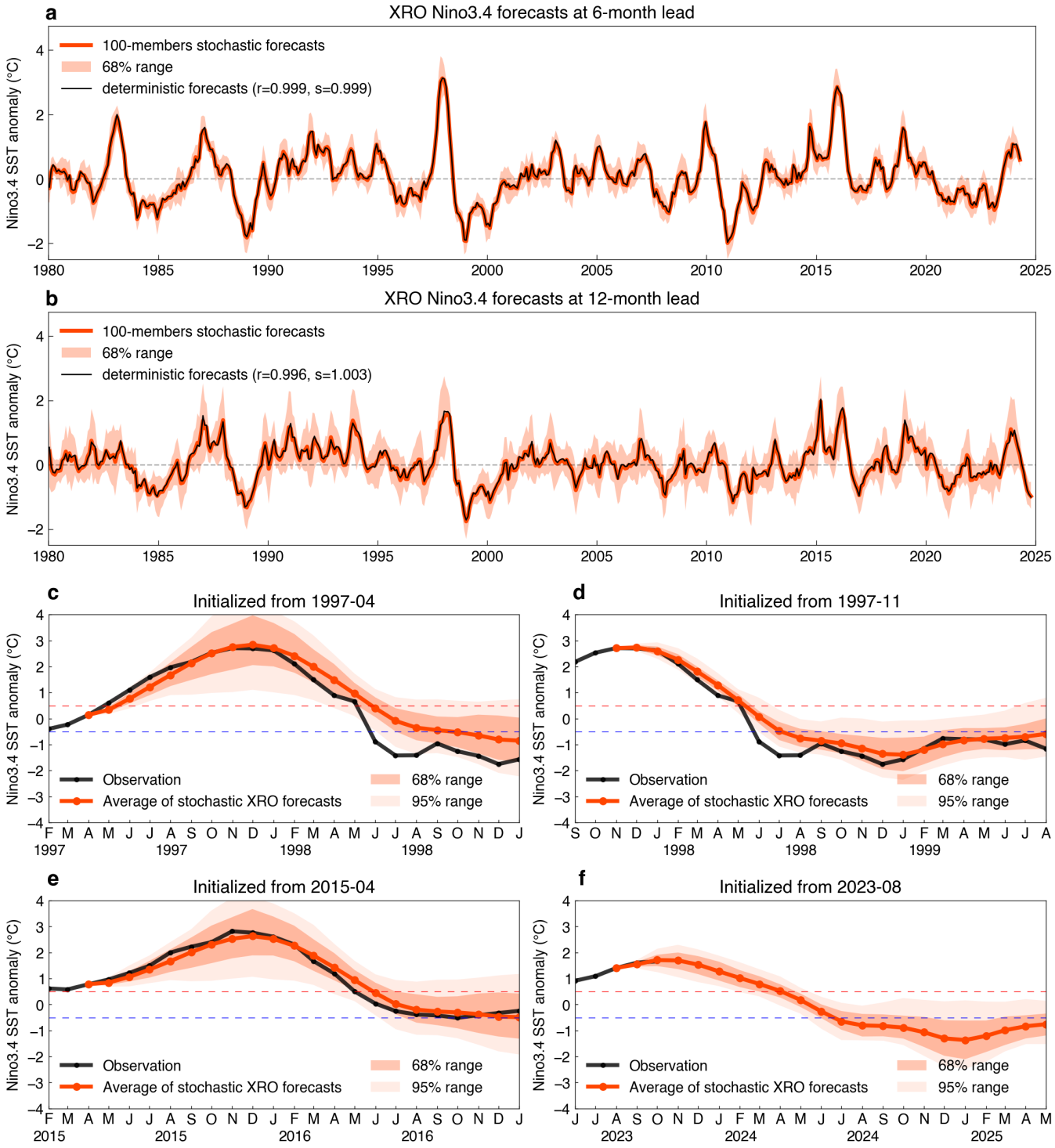

Supplementary Fig. 16| 100-member stochastic forecasts of ENSO by the XRO. a-b, Time series of XRO-forecasted Niño3.4 SSTA, at lead-times of (a) 6 months and (b) 12 months. Black curves correspond to a deterministic forecast, in which the stochastic forcing term is neglected during the integration. Forecasts from a 100-member stochastic XRO ensemble are shown in red (dark red for the ensemble mean, red shadings indicate the central 68% range of the ensemble members). The correlation and regression slope between the deterministic forecast and the stochastic ensemble mean are indicated in the

corresponding legends. **c-f**, Niño3.4 SSTA forecasts initialized in (a) 1997 April, (b) 1997 November, (c) 2015 April, and (d) 2023 August. Red curves show the ensemble-mean XRO forecast; dark red envelope is the central 68% range of the ensemble members; lighter red is the central 95% range; black curves show the observations. The ensemble mean of the XRO stochastic forecasts is almost identical to the deterministic XRO forecast. The XRO stochastic forecasts provide an opportunity for probabilistic ENSO forecasts. The seasonality of the ENSO growth rate leads to a substantial spread in forecast outcomes from November to February. This inherent spread reflects a higher degree of uncertainty in predicting the peak amplitude of ENSO during this period. Conversely, from April to June, the forecast spread is narrower. However, this does not necessarily imply a better forecast skill, as the actual signal during this period is quite weak, resulting in a low signal-to-noise ratio.

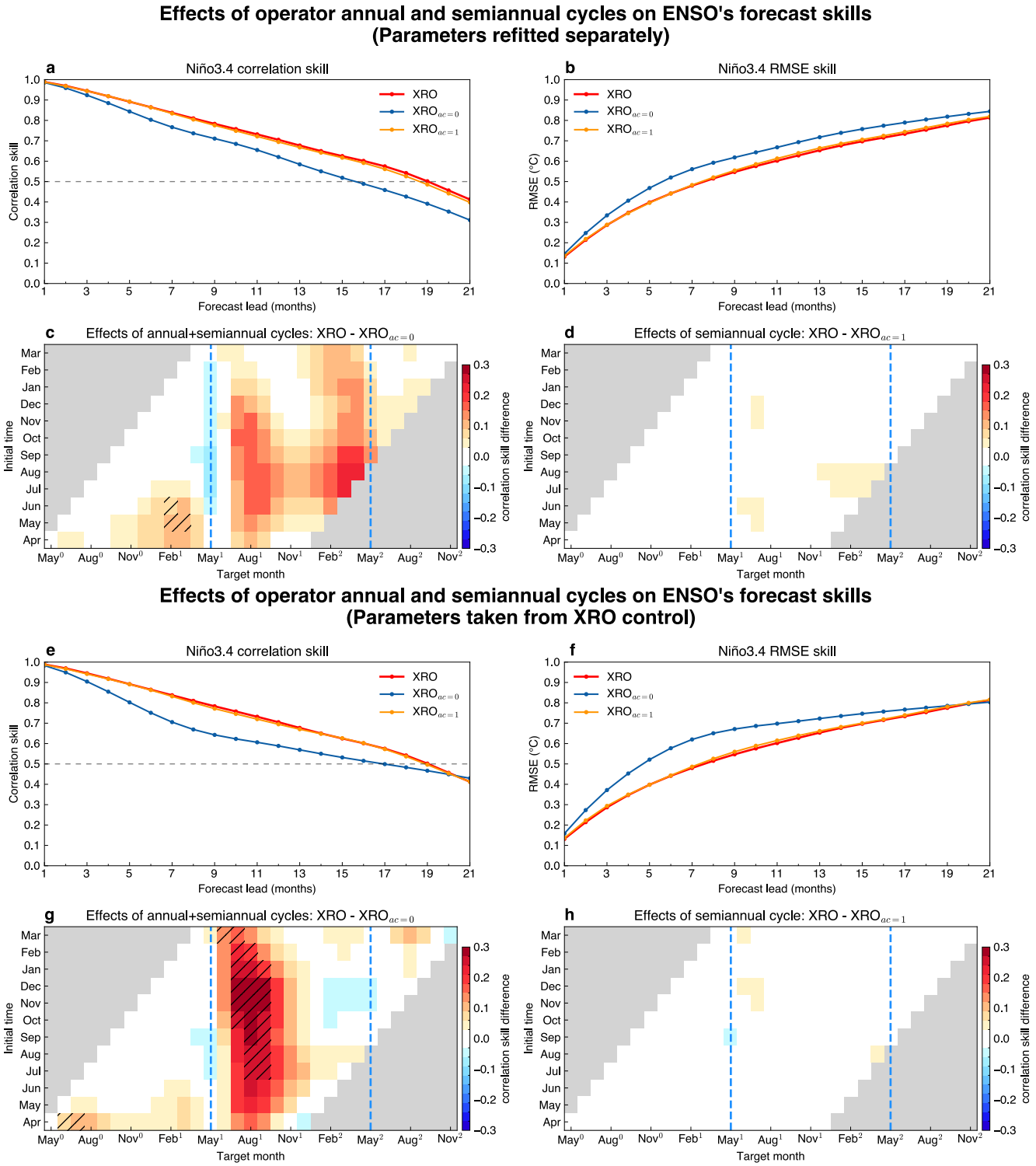

Supplementary Fig. 17| Effects of the XRO operator's annual and semiannual cycles on its ENSO forecast skill during 1979-2022. a-b, The all-months (a) correlation skill and (b) RMSE of the forecasted 3-month running mean Niño3.4 SSTA index, as a function of forecast lead, for the XRO in which the annual mean, annual cycle, and semiannual components are all considered in the linear and nonlinear parameters (*red*), $XRO_{ac=0}$ in which only the annual mean component is considered (*blue*), and $XRO_{ac=1}$

in which both the annual mean and annual cycle components are considered (*orange*). **c-d**, the skill difference of the Niño3.4 index, as a function of start month (ordinate) and target month (abscissa), between XRO and the deseasonalized experiments: (c) $XRO_{ac=0}$ and (d) $XRO_{ac=1}$. Hatching indicates that the correlation difference is significant at 90% confidence level using the two-tailed Fisher z-transformation test. The dashed vertical blue lines denote the spring predictability barrier (SPB) season. **a-d,** the parameters for $XRO_{ac=0}$ and $XRO_{ac=1}$ are refitted separately; **e-h**, same as **a-d**, but for $XRO_{ac=0}$ and $XRO_{ac=1}$ in which the parameters are taken from the XRO control experiment. The seasonal cycle is critically important for suppressing the SPB for ENSO, while the semi-annual cycle is less important.

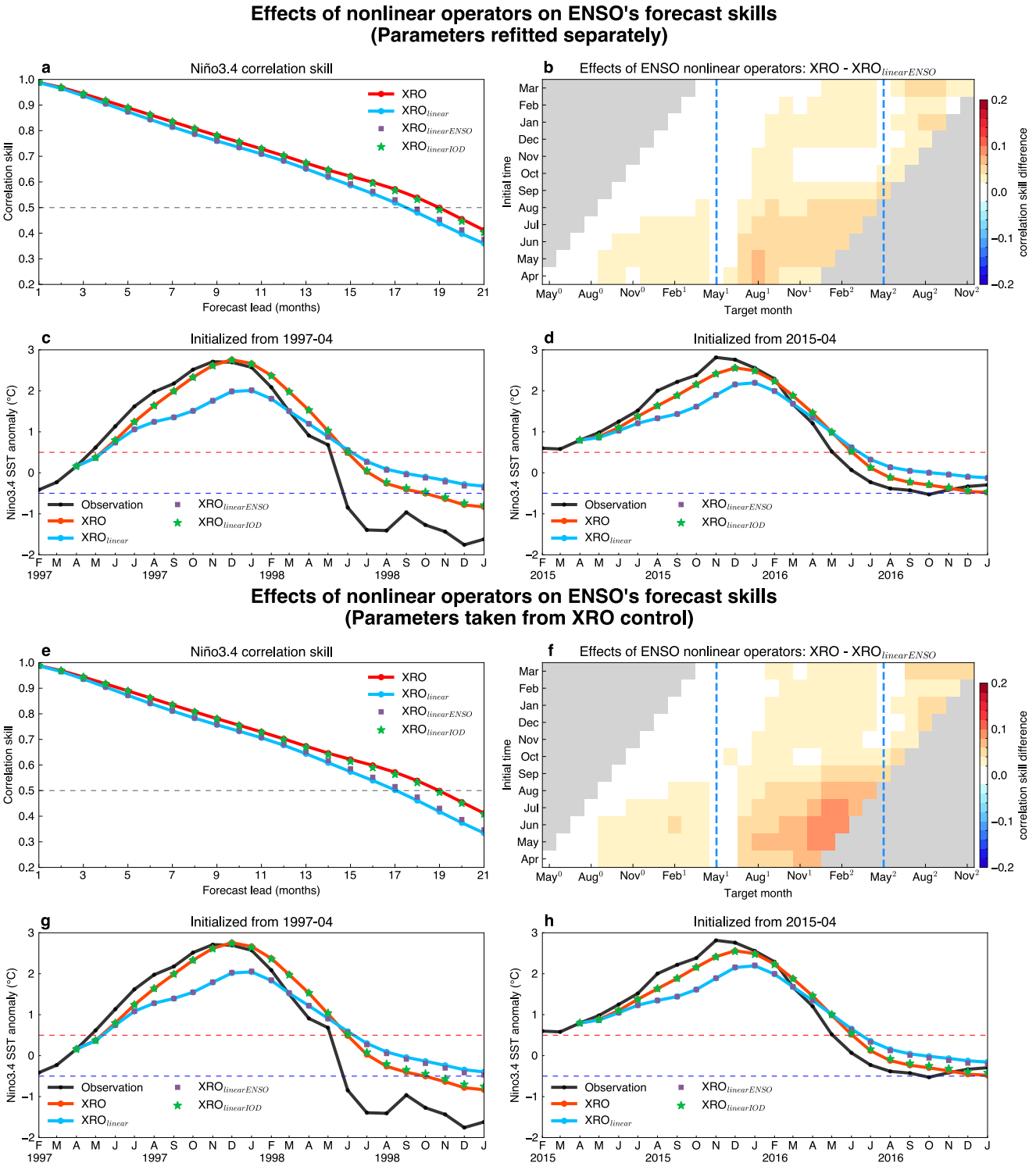

Supplementary Fig. 18| Effects of the XRO nonlinear operators on its ENSO forecast skill during 1979-2022. a, The all-months (a) correlation skill of the forecasted 3-month running mean Niño3.4 SSTA index, as a function of forecast lead for the XRO control (*red*), XRO$_{\text{linear}}$ (*blue*), XRO$_{\text{linearENSO}}$ (*purple square*), and XRO$_{\text{linearIOD}}$ (*green stars*). **b**, the skill difference of the Niño3.4 index, as a function of start month (ordinate) and target month (abscissa), between XRO and XRO$_{\text{linearENSO}}$. The dashed vertical blue lines denote the spring predictability barrier season. **c-d**, monthly Niño3.4 SSTA forecasts initialized in

(a) 1997 April and (b) 2015 April for the XRO control (*red*), XRO_{linear} (*blue*), $XRO_{linearENSO}$ (*purple square*), and $XRO_{linearIOD}$ (*green star*s); black curves show the observations. **a-d,** the parameters for XRO_{linear}, $XRO_{linearENSO}$, and $XRO_{linearIOD}$ are refitted separately; **e-h**, same as **a-d**, but for XRO_{linear}, $XRO_{linearENSO}$, and $XRO_{linearIOD}$ in which the parameters are taken from the XRO control experiment. The ENSO nonlinear dynamics are critically important for ENSO forecast skill, especially for forecasting the amplitude of the peak phase and fast transition from El Niño to La Niña. The impact of the IOD's nonlinearity on ENSO forecast skill is neglectable.

References in Supplementary Information

An, S.-I., and F.-F. Jin, 2004: Nonlinearity and Asymmetry of ENSO. *J. Climate*, **17**, 2399–2412, https://doi.org/10.1175/1520-0442(2004)017<2399:NAAOE>2.0.CO;2.

An, S.-I., E. Tziperman, Y. M. Okumura, and T. Li, 2020: ENSO Irregularity and Asymmetry. *El Niño Southern Oscillation in a Changing Climate*, American Geophysical Union (AGU), 153–172.

An, S.-I., H.-J. Park, S.-K. Kim, W. Cai, A. Santoso, D. Kim, and J.-S. Kug, 2023: Main drivers of Indian Ocean Dipole asymmetry revealed by a simple IOD model. *npj Clim Atmos Sci*, **6**, 1–7, https://doi.org/10.1038/s41612-023-00422-2.

Behringer, D., and Y. Xue, 2004: Evaluation of the global ocean data assimilation system at NCEP: The Pacific Ocean. *Eighth Symposium on Integrated Observing and Assimilation Systems for Atmosphere, Oceans, and Land Surface*, Vol. 2.3 of, AMS 84th Annual Meeting, Washington, 11–15.

de Boisséson, E., M. A. Balmaseda, and M. Mayer, 2018: Ocean heat content variability in an ensemble of twentieth century ocean reanalyses. *Clim Dyn*, **50**, 3783–3798, https://doi.org/10.1007/s00382-017-3845-0.

Carton, J. A., and B. S. Giese, 2008: A Reanalysis of Ocean Climate Using Simple Ocean Data Assimilation (SODA). *Mon. Wea. Rev.*, **136**, 2999–3017, https://doi.org/10.1175/2007MWR1978.1.

Chen, H.-C., and F.-F. Jin, 2021: Simulations of ENSO Phase-Locking in CMIP5 and CMIP6. *Journal of Climate*, **34**, 5135–5149, https://doi.org/10.1175/JCLI-D-20-0874.1.

Chen, H.-C., F.-F. Jin, and L. Jiang, 2021: The Phase-Locking of Tropical North Atlantic and the Contribution of ENSO. *Geophysical Research Letters*, **48**, e2021GL095610, https://doi.org/10.1029/2021GL095610.

Choi, K.-Y., G. A. Vecchi, and A. T. Wittenberg, 2013: ENSO Transition, Duration, and Amplitude Asymmetries: Role of the Nonlinear Wind Stress Coupling in a Conceptual Model. *J. Climate*, **26**, 9462–9476, https://doi.org/10.1175/jcli-d-13-00045.1.

DiNezio, P. N., and C. Deser, 2014: Nonlinear Controls on the Persistence of La Niña. *J. Climate*, **27**, 7335–7355, https://doi.org/10.1175/JCLI-D-14-00033.1.

Ding, R., Y.-H. Tseng, E. Di Lorenzo, L. Shi, J. Li, J.-Y. Yu, C. Wang, C. Sun, J.-J. Luo, K.-J. Ha, Z.-Z. Hu, and F. Li, 2022: Multi-year El Niño events tied to the North Pacific Oscillation. *Nat Commun*, **13**, 3871, https://doi.org/10.1038/s41467-022-31516-9.

Enfield, D. B., A. M. Mestas-Nuñez, D. A. Mayer, and L. Cid-Serrano, 1999: How ubiquitous is the dipole relationship in tropical Atlantic sea surface temperatures? *Journal of Geophysical Research: Oceans*, **104**, 7841–7848, https://doi.org/10.1029/1998JC900109.

Geng, T., W. Cai, and L. Wu, 2020: Two Types of ENSO Varying in Tandem Facilitated by Nonlinear Atmospheric Convection. *Geophysical Research Letters*, **47**, e2020GL088784, https://doi.org/10.1029/2020GL088784.

Geng, T., F. Jia, W. Cai, L. Wu, B. Gan, Z. Jing, S. Li, and M. J. McPhaden, 2023: Increased occurrences of consecutive La Niña events under global warming. *Nature*, **619**, 774–781, https://doi.org/10.1038/s41586-023-06236-9.

Hersbach, H., B. Bell, P. Berrisford, S. Hirahara, A. Horányi, J. Muñoz-Sabater, J. Nicolas, C. Peubey, R. Radu, D. Schepers, A. Simmons, C. Soci, S. Abdalla, X. Abellan, G. Balsamo, P. Bechtold, G. Biavati, J. Bidlot, M. Bonavita, G. De Chiara, P. Dahlgren, D. Dee, M. Diamantakis, R. Dragani, J. Flemming, R. Forbes, M. Fuentes, A. Geer, L. Haimberger, S. Healy, R. J. Hogan, E. Hólm, M. Janisková, S. Keeley, P. Laloyaux, P. Lopez, C. Lupu, G. Radnoti, P. de Rosnay, I. Rozum, F. Vamborg, S. Villaume, and J.-N. Thépaut, 2020: The ERA5 global reanalysis. *Quarterly Journal of the Royal Meteorological Society*, **146**, 1999–2049, https://doi.org/10.1002/qj.3803.

Hirahara, S., M. Ishii, and Y. Fukuda, 2014: Centennial-Scale Sea Surface Temperature Analysis and Its Uncertainty. *Journal of Climate*, **27**, 57–75, https://doi.org/10.1175/JCLI-D-12-00837.1.

Huang, B., P. W. Thorne, V. F. Banzon, T. Boyer, G. Chepurin, J. H. Lawrimore, M. J. Menne, T. M. Smith, R. S. Vose, and H.-M. Zhang, 2017: Extended Reconstructed Sea Surface Temperature, Version 5 (ERSSTv5): Upgrades, Validations, and Intercomparisons. *Journal of Climate*, **30**, 8179–8205, https://doi.org/10.1175/JCLI-D-16-0836.1.

Iwakiri, T., and M. Watanabe, 2021: Mechanisms linking multi-year La Niña with preceding strong El Niño. *Sci Rep*, **11**, 17465, https://doi.org/10.1038/s41598-021-96056-6.

Iwakiri, T., and M. Watanabe, 2022: Multiyear ENSO Dynamics as Revealed in Observations, Climate Model Simulations, and the Linear Recharge Oscillator. *Journal of Climate*, **35**, 7625–7642, https://doi.org/10.1175/JCLI-D-22-0108.1.

Jeong, H., H.-S. Park, M. F. Stuecker, and S.-W. Yeh, 2022: Distinct impacts of major El Niño events on Arctic temperatures due to differences in eastern tropical Pacific sea surface temperatures. *Science Advances*, **8**, eabl8278, https://doi.org/10.1126/sciadv.abl8278.

Jiang, F., W. Zhang, F.-F. Jin, M. F. Stuecker, A. Timmermann, M. J. McPhaden, J. Boucharel, and A. T. Wittenberg, 2023: Resolving the Tropical Pacific/Atlantic Interaction Conundrum. *Geophysical Research Letters*, **50**, e2023GL103777, https://doi.org/10.1029/2023GL103777.

Jo, H.-S., Y.-G. Ham, J.-S. Kug, T. Li, J.-H. Kim, J.-G. Kim, and H. Kim, 2022: Southern Indian Ocean Dipole as a trigger for Central Pacific El Niño since the 2000s. *Nat Commun*, **13**, 6965, https://doi.org/10.1038/s41467-022-34721-8.

Kang, I.-S., and J.-S. Kug, 2002: El Niño and La Niña sea surface temperature anomalies: Asymmetry characteristics associated with their wind stress anomalies. *Journal of Geophysical Research: Atmospheres*, **107**, ACL 1-1-ACL 1-10, https://doi.org/10.1029/2001JD000393.

Kim, J.-W., and J.-Y. Yu, 2022: Single- and multi-year ENSO events controlled by pantropical climate interactions. *npj Clim Atmos Sci*, **5**, 1–11, https://doi.org/10.1038/s41612-022-00305-y.

Kim, J.-W., J.-Y. Yu, and B. Tian, 2023: Overemphasized role of preceding strong El Niño in generating multi-year La Niña events. *Nat Commun*, **14**, 6790, https://doi.org/10.1038/s41467-023-42373-5.

Köhl, A., 2020: Evaluating the GECCO3 1948–2018 ocean synthesis – a configuration for initializing the MPI-ESM climate model. *Quarterly Journal of the Royal Meteorological Society*, **146**, 2250–2273, https://doi.org/10.1002/qj.3790.

Levine, A. F. Z., and M. J. McPhaden, 2015: The annual cycle in ENSO growth rate as a cause of the spring predictability barrier. *Geophysical Research Letters*, **42**, 5034–5041, https://doi.org/10.1002/2015GL064309.

Nnamchi, H. C., J. Li, F. Kucharski, I.-S. Kang, N. S. Keenlyside, P. Chang, and R. Farneti, 2015: Thermodynamic controls of the Atlantic Niño. *Nature Communications*, **6**, 8895, https://doi.org/10.1038/ncomms9895.

Okumura, Y. M., M. Ohba, C. Deser, and H. Ueda, 2011: A Proposed Mechanism for the Asymmetric Duration of El Niño and La Niña. *Journal of Climate*, **24**, 3822–3829, https://doi.org/10.1175/2011JCLI3999.1.

Park, J.-H., S.-I. An, J.-S. Kug, Y.-M. Yang, T. Li, and H.-S. Jo, 2021: Mid-latitude leading double-dip La Niña. *International Journal of Climatology*, **41**, E1353–E1370, https://doi.org/10.1002/joc.6772.

Rayner, N. A., D. E. Parker, E. B. Horton, C. K. Folland, L. V. Alexander, D. P. Rowell, E. C. Kent, and A. Kaplan, 2003: Global analyses of sea surface temperature, sea ice, and night marine air temperature since the late nineteenth century. *Journal of Geophysical Research: Atmospheres*, **108**, https://doi.org/10.1029/2002JD002670.

Richter, I., M. F. Stuecker, N. Takahashi, and N. Schneider, 2022: Disentangling the North Pacific Meridional Mode from tropical Pacific variability. *npj Clim Atmos Sci*, **5**, 1–9, https://doi.org/10.1038/s41612-022-00317-8.

Rodrigues, R. R., E. J. D. Campos, and R. Haarsma, 2015: The Impact of ENSO on the South Atlantic Subtropical Dipole Mode. *Journal of Climate*, **28**, 2691–2705, https://doi.org/10.1175/JCLI-D-14-00483.1.

Saji, N. H., B. N. Goswami, P. N. Vinayachandran, and T. Yamagata, 1999: A dipole mode in the tropical Indian Ocean. *Nature*, **401**, 360–363, https://doi.org/10.1038/43855.

Stein, K., A. Timmermann, N. Schneider, F.-F. Jin, and M. F. Stuecker, 2014: ENSO Seasonal Synchronization Theory. *J. Climate*, **27**, 5285–5310, https://doi.org/10.1175/JCLI-D-13-00525.1.

Trenberth, K. E., 1997: The Definition of El Niño. *Bulletin of the American Meteorological Society*, **78**, 2771–2778, https://doi.org/10.1175/1520-0477(1997)078<2771:TDOENO>2.0.CO;2.

Xie, P. P., and P. A. Arkin, 1997: Global precipitation: A 17-year monthly analysis based on gauge observations, satellite estimates, and numerical model outputs. *Bull. Amer. Meteor. Soc.*, **78**, 2539–2558, https://doi.org/10.1175/1520-0477(1997)078<2539:Gpayma>2.0.Co;2.

Xie, S.-P., K. M. Hu, J. Hafner, H. Tokinaga, Y. Du, G. Huang, and T. Sampe, 2009: Indian Ocean capacitor effect on Indo-Western Pacific climate during the summer following El Niño. *J. Climate*, **22**, 730–747, https://doi.org/10.1175/2008jcli2544.1.

Yin, Y., O. Alves, and P. R. Oke, 2011: An Ensemble Ocean Data Assimilation System for Seasonal Prediction. *Mon. Wea. Rev.*, **139**, 786–808, https://doi.org/10.1175/2010MWR3419.1.

Zhang, H., A. Clement, and P. D. Nezio, 2014: The South Pacific Meridional Mode: A Mechanism for ENSO-like Variability. *Journal of Climate*, **27**, 769–783, https://doi.org/10.1175/JCLI-D-13-00082.1.

Zhao, S., F.-F. Jin, and M. F. Stuecker, 2021: Understanding Lead Times of Warm Water Volumes to ENSO Sea Surface Temperature Anomalies. *Geophysical Research Letters*, **48**, e2021GL094366, https://doi.org/10.1029/2021GL094366.

Zuo, H., M. A. Balmaseda, S. Tietsche, K. Mogensen, and M. Mayer, 2019: The ECMWF operational ensemble reanalysis–analysis system for ocean and sea ice: a description of the system and assessment. *Ocean Science*, **15**, 779–808, https://doi.org/10.5194/os-15-779-2019.